RSC Advances

Morphology and dopant-dependent optical characteristics of novel composite 1D and 3D-based heterostructures of CdSe nanocrystals and LaPO4: Re (Re = Eu, Ce, Tb) metal phosphate nanowires

Journal:	*RSC Advances*
Manuscript ID:	RA-ART-06-2014-005933
Article Type:	Paper
Date Submitted by the Author:	18-Jun-2014
Complete List of Authors:	Han, Jinkyu; Brookhaven National Lab, Wang, Lei; SUNY Stony Brook, Wong, Stanislaus S; SUNY Stony Brook,

Morphology and dopant-dependent optical characteristics of novel composite 1D and 3D-based heterostructures of CdSe nanocrystals and $LaPO_4$: Re (Re = Eu, Ce, Tb) metal phosphate nanowires

Jinkyu Han[1], Lei Wang[2], and Stanislaus S. Wong[1,2,*]

[1]Condensed Matter Physics and Materials Sciences Department, Building 480, Brookhaven National Laboratory, Upton NY 11973

[2] Department of Chemistry, State University of New York at Stony Brook, Stony Brook, NY 11794-3400

*To whom correspondence should be addressed.

Email: sswong@bnl.gov, stanislaus.wong@stonybrook.edu

Abstract

In this report, we synthesize and structurally characterize novel semiconducting nanoscale composite heterostructures composed of zero-dimensional (0D) CdSe nanocrystals coupled with both one-and three-dimensional (1D and 3D) rare earth metal-doped $LaPO_4$ metal phosphate materials. Subsequent optical characterization has demonstrated a clear dependence of the intrinsic charge and energy transfer processes in these systems on both (i) morphology and (ii) the presence of dopants. Specifically, ~4.5 nm CdSe quantum dots (QDs) have been successfully anchored onto (a) high-aspect ratio rare-earth activated $LaPO_4$ nanowires, measuring ~7 nm in diameter and ~1.3 μm in length, prepared by a modified hydrothermal protocol, and (b) well-dispersed urchin-like 3D architectures of $LaPO_4$: Re (Re = Ce, Tb, Eu) (diameter ~500 nm), fabricated using a large-scale, solution-precipitation approach in the presence of 6-mercaptohexanoic acid, used as a self-assembly facilitating agent. We have proposed a growth mechanism of our 3D sub-micron $LaPO_4$-based architectures, based on a detailed time-dependent scanning electron microscopy visualization study. In terms of properties, our results show that our 1D and 3D heterostructures evince both PL quenching and a shorter average lifetime of CdSe QDs as compared with unbound CdSe QDs. We suggest that a photo-induced charge transfer process occurs from CdSe QDs to $LaPO_4$: Eu through the mediation of water molecules in the intrinsic $LaPO_4$ structure. Conversely, analogous CdSe QD- 3D $LaPO_4$: Eu heterostructures exhibit noticeably less PL quenching and longer lifetimes as compared with 1D composites since it appears that not only charge transfer from CdSe to $LaPO_4$: Eu but also energy transfer from $LaPO_4$: Eu to CdSe QDs are substantially more efficient processes with 3D as compared with 1D heterostructures, possibly due to the nearly 3 times higher coverage density of QDs on the surfaces of the underlying 3D $LaPO_4$ motif, thereby contributing to its more effective absorption capability of $LaPO_4$: Eu emission. Moreover, the magnitude of the PL signal and the corresponding lifetimes in the CdSe QD (0D) - $LaPO_4$ (3D) heterostructures are dependent upon the rare-earth dopant tested itself. Data are additionally explained in the context of the inherent energy level alignments of both CdSe QDs and $LaPO_4$: Re (Re = Ce, Tb, and Eu) systems.

1. Introduction

There have been innumerable reports concerning the size and morphology dependence of the intrinsic physical characteristics of nanomaterials.[1-8] Apart from gaining fundamental insights into structure-property correlations, the underlying objective of many of these studies has been a quasi-quixotic quest to be able to rationally tailor nanomaterials essentially from scratch to take advantage of their unique and distinctive optical, electronic, catalytic, and physico-chemical properties. Indeed, the capability of doing so would have important implications for the creation of functional devices. One practical prerequisite to achieving this goal has been the need to synthesize pure and monodisperse samples of controlled composition and morphology. In this light, extensive research has focused on creating not only standard zero-dimensional (0D) nanoparticle as well as one-dimensional (1D) nanowire and nanotube motifs but also more unusual two-dimensional (2D) nanoplates and three-dimensional (3D) urchin-like architectures via a number of interesting strategies.[9-11]

Moreover, through our prior work on carbon nanotube (CNT) - quantum dot (QD) heterostructures,[12-16] we subscribe to the philosophical approach that the unique and desirable properties of individual nanostructures can be significantly enhanced in potentially unforeseen ways through the formation of nanoscale heterostructures composed of different, distinctive, and complementary constituent subunits. The idea is that the properties of the composite whole are often unexpected and sometimes enhanced as compared with its individual component parts. For example, the size dependent optical and electronic properties of QDs can be ‘re-defined’ and ‘re-tooled’ in the context of nanoscale QD-based heterostructures, such as CdS QD- bulk Bi_2WO_6 composites[17] and CdS QD-1D Fe_2O_3 systems.[18] In particular, these novel materials can enhance the migratory efficiency of photo-generated carriers, thereby resulting in the improvement of

photocatalytic activity. By analogy, heterostructures involving QDs purposely coupled either with TiO_2, ZnO, or CNTs can be used to improve charge separation and transport capabilities for solar cell applications.[19-23]

More recently, this concept of combining distinctive chemical components has been extended to studies of (i) QDs attached to various luminescent dyes and inorganic complexes, such as CdTe QD-*meso*-tetra(4-sulfonatophenyl) porphine dihydrochloride and CdSe QD-Ru-polypyridine, (ii) QDs linked with biologically active moieties such as CdSe QD-Eu, Tb-doped streptavidin complexes, and (iii) QDs bound to rare-earth doped inorganic materials, such as CdSe QD–$NaYF_4$: Yb, Er nanocrystals and CdS-$LaPO_4$: Eu^{3+} core-shell nanowires.[24-27] These examples highlight the synthetic potential to design and tailor optical properties, such as charge and energy transfer between the two components, within carefully engineered heterostructures.

Our specific study therefore is significant for 2 reasons. *First*, we highlight and focus on creating pure and well-defined nanoscale building blocks, such as luminescent CdSe QDs and rare earth activated $LaPO_4$ nanoscale motifs. *Second*, by creating more nuanced nanoscale architectures, composed of different, mixed morphologies such as 0D-1D and 0D-3D composites, we demonstrate the crucial role of nanostructure morphology in dictating the opto-electronic properties of the resulting heterostructure.[5-8] In terms of recent, relevant prior work, our group has reported on novel distinctive nanoscale heterostructures, comprised of CdSe QDs attached to either $CePO_4$: Tb 0D nanoparticles or 1D nanowires. We observed noticeable luminescence quenching and shortened PL lifetimes in these coupled composites as compared with their free, unbound components, due to either charge transfer from CdSe QDs to $CePO_4$: Tb or vice versa, as a function of the excitation wavelength.[28] In the current study, we generate for the first time novel 0D QD-1D as well as 0D QD-3D $LaPO_4$-based heterostructures. We note a clear

dependence not only of morphology but also of dopant identity upon the resulting optical behavior of these composite heterostructures. From a structure-property correlation point of view, creating heterostructures based on combining CdSe QDs with the lesser known $LaPO_4$: Re (Eu, Ce, Tb) 1D nanowires and 3D urchin-like architectures can potentially generate a new class of functional luminescent materials.

Specifically, rare earth doped $LaPO_4$ has been extensively used as an emitting material in fluorescent lamps and has also been considered for optoelectronics,[29-31] due to its lower photo-bleaching capability, high quantum yields (up to 90% at deep UV excitation), reasonable chemical stability, and relatively low toxicity. Indeed, the strong UV (Ce^{3+}), green (Tb^{3+}), and red (Eu^{3+}) emission bands, resulting from the unique 4*f* electron configuration of rare earth dopants, can be observed upon UV excitation in the range of 250-280 nm.[32] To date, various lanthanide orthophosphates possessing different morphologies, such as 0D nanocrystals, 1D nanotubes or nanowires, and more complex core/shell structures, have been successfully synthesized using a number of different methods, including sol-gel, co-precipitation, hydrothermal, electrospinning, and microemulsion protocols.[33-37] In terms of 1D nanowires of lanthanide orthophosphate, their preparation has focused on either a conventional or a modified hydrothermal protocol.[38-40] Due to the intrinsic crystal structural properties of lanthanide phosphate, its uniaxial growth is relatively facile and well understood.[39]

By contrast, it is still reasonably challenging to easily obtain 3D hierarchical structures of phosphate-based materials such as (La, Ce, Bi, Gd)PO_4.[41-45] Moreover, the growth mechanism for these 3D assemblies is still relatively unknown, and related time-dependent kinetic studies of such a formation process at the nanoscale are correspondingly few. Therefore, as a novel contribution to nanoscale synthesis herein, we have devised a facile, template-free, ambient, and

aqueous solution-directed synthetic route using 6-mercaptohexanoic acid (MHA) as a self-assembly facilitating agent for the large-scale production of sub-micron rare earth-doped hierarchical 3D $LaPO_4$ structures, which are considerably smaller as compared with other analogous 3D phosphate-based materials, which typically measure over 3 μm in diameter.[36, 43-45] Furthermore, we have proposed a growth mechanism of our 3D sub-micron $LaPO_4$-based architectures from interpretation of a detailed time-dependent scanning electron microscopy visualization study. We essentially demonstrate that 3D hierarchical structures of lanthanide phosphate can be constructed from the controlled organization of 1D nanoscale building blocks, possessing tailored chemical components and controlled morphologies.

Based on these building blocks (i.e. as-prepared 1D and 3D rare earth doped $LaPO_4$ and semiconducting CdSe QDs), we have successfully achieved the synthesis and subsequent optical characterization of 0D QD - luminescent rare earth activated metal oxide (e.g. lanthanum phosphate) architectures. Specifically, we have created a unique family of 0D CdSe QD - 1D/3D rare earth doped $LaPO_4$ heterostructures, thereby coupling and taking advantage of the intrinsically interesting optoelectronic properties of constituent nanomaterials. In particular, in terms of achieving efficient and suggestive structure-property correlations so as to gain a fundamental understanding of our system, we have interpreted optical absorption, luminescence (i.e. emission) behavior, as well as the corresponding lifetimes of different morphological variants of these CdSe QD-$LaPO_4$ heterostructures in the context of tunable synthetic parameters, such as morphology, QD coverage density, and the presence of $LaPO_4$ dopants (i.e. Ce, Eu, Tb). Moreover, our efforts are likely to be of general interest for the development of potentially distinctive and novel structural designs for photovoltaic and solar cell architectures.

2. Experimental

2.1. Synthesis.

2.1.1. 1D structures of $LaPO_4$: Eu

Doped $LaPO_4$: Eu nanowires have been prepared according to a well known and previously reported hydrothermal approach.[38-40] Briefly, 1 mmol of $La(NO_3)_3 \cdot 6H_2O$ and 0.05 mol of $Eu(NO_3)_3 \cdot 6H_2O$ were dissolved in 10 ml deionized water so as to generate the desired Eu-doped $LaPO_4$ nanostructures. Subsequently, 1 mmol of H_3PO_4 in 10 ml aqueous solution was added to the mixture in order to assist in the precipitation of $LaPO_4$: Eu, with the ultimate expected La: Eu: P molar ratio intended to be 1: 0.05: 1. The solution was then vigorously stirred for 30 min. The final solution was transferred into a Teflon-lined stainless-steel autoclave (capacity of 50 mL) and sealed. The autoclave was subsequently heated at 100°C for 8 h, and cooled naturally to room temperature. As-prepared, hydrated phosphate nanowires were later isolated from solution by centrifugation upon washing with water and ethanol (EtOH), and later air dried at 80°C for 12 h. Finally, as-prepared nanowires were post-annealed at 400°C for 1 h in air so as to improve their crystallinity, which has an impact upon the resulting luminescence output of $LaPO_4$: Eu.

2.1.2. 3D structures of $LaPO_4$: Re (Re = Eu, Ce, and Tb)

A typical synthesis of urchin-like 3D hierarchical structure of $LaPO_4$: Re (Re = Ce, Tb, and Eu) was performed using hydrated metallic precursors in solution using MHA as a self-assembly facilitating agent for the formation of 3D architectures. In a representative ambient protocol, 10 mL of an aqueous mixture of 0.5 mmol of $La(NO_3)_3 \cdot 6H_2O$ and either 0.025 mmol $Eu(NO_3)_3 \cdot 6H_2O$, $Tb(NO_3)_3 \cdot 6H_2O$, or $Ce(NO_3)_3 \cdot 5H_2O$ was prepared so as to yield a final molar dopant concentration of ~5.0 weight %. Subsequently, 1.5 mmol of MHA in aqueous solution

was added to the resulting mixture under strong magnetic stirring with the corresponding and immediate formation of white flocculant. The molar ratio of La to MHA was fixed at a stoichiometric ratio of 1: 3. We believe the flocculant was most likely $La(MHA)_3$, since COO^- can react with metal ions, including rare-earth ions, so as to produce a compound of $M(COO)_n$.[46] Subsequently, 1 mmol of H_3PO_4 in 10 ml aqueous solution was added slowly, and the flocculant became a white precipitate. After stirring vigorously for 1 h, the precipitate was collected by centrifugation and washed with deionized water and ethanol for several times. The final products were air dried at 80°C for 12 h. By analogy with the 1D structures, as-prepared 3D urchin-like structures were post-annealed at 400°C for 1 h in air.

2.1.3. CdSe QDs and Composite heterostructures of CdSe QD - 1D/3D $LaPO_4$: Eu

Colloidal CdSe QDs were prepared using a modified literature protocol.[47] In brief, 0.2 mmol CdO and 0.8 mmol of stearic acid were degassed at 150°C, and then heated under an Ar atmosphere in order to completely dissolve the precursors in a three-neck flask. We note that stearic acid can assist in generating CdSe QDs over a very broad size range, without the need for any secondary injection, from about 2 nm to over 25 nm. Subsequently, 3.88 g each of trioctylphosphine oxide (TOPO) and hexadecylamine (HDA), which were used as capping molecules for the generation of nanocrystals possessing a high quantum yield, were added to the flask, and the mixture was heated to 320°C. In parallel, in an air-sensitive glovebox environment, 2 mmol of Se were dissolved in tributylphosphine (TBP) as well as in the presence of dioctylamine (DOA). It is thought that DOA can potentially mitigate against the toxicity of the TBP-Se solution. The Se solution was then injected into the hot metallic precursor solution at 320°C, and subsequent QD growth was carried out at 270°C for 15 s. The mixture was later

allowed to cool to room temperature, and it was washed with a solution of either methanol (MeOH) or acetone, prior to dissolution in hexane.

CdSe QDs capped with 2-aminoethanethiol (AET), a well-known hole scavenging agent for CdSe QDs, were obtained through a ligand exchange reaction. In a typical experiment, a solution of AET (1 mmol) in 2 ml of MeOH was added to a suspension of as-prepared, capped CdSe QDs (0.04 mmol) in 4 ml of hexane. After stirring for 10 min, QDs were precipitated upon ligand exchange. These QDs were later collected by centrifugation and then washed with both ethanol and MeOH. The resulting QDs were finally re-dispersed in MeOH for future use.

AET-capped CdSe QDs were attached onto either $LaPO_4$: Eu 1D nanowires or 3D urchin-like sub-micron $LaPO_4$: Re (Re = Ce, Tb, and Eu) architectures presumably through a hydrogen bonding mechanism, involving water molecules intercalated within the $LaPO_4$: Re hexagonal structure, in an analogous manner to our previous report of CdSe QDs attached onto $CePO_4$: Tb nanowires.[28] For example, in a typical experiment, 2.4 mg (10.4 μmol) of $LaPO_4$: Eu in 2 ml MeOH was added to 2 mg (10.4 μmol) of AET-capped CdSe QDs in 2 ml of MeOH. The resulting solution was then sonicated for 10 min and stirred in the dark for 2 h in order to preserve optical integrity. These heterostructures were subsequently washed with MeOH, and ultimately re-dispersed in MeOH prior to further use and analysis.

2.2. Characterization

Samples were thoroughly characterized using a number of different complementary methodologies, including powder X-ray diffraction (XRD), Fourier transform infrared spectroscopy (FTIR), scanning electron microscopy (SEM), transmission electron microscopy (TEM), energy-dispersive X-ray spectroscopy (EDS), high resolution TEM (HRTEM), as well as

UV-visible spectroscopy, steady-state photoluminescence (PL) spectroscopy, and time-resolved fluorescence lifetime spectroscopy.

2.2.1. X-ray Diffraction.

Crystallographic and purity information on the CdSe QDs and the corresponding $LaPO_4$: Eu 1D nanowires and 3D sub-micron-scale architectures were initially obtained using powder X-ray diffraction. To prepare the relevant samples for analysis, the resulting QDs, 1D nanowires, and 3D urchin-like architectural samples were rendered into slurries, i.e. in chloroform for QDs and in ethanol for both 1D and 3D structures of $LaPO_4$: Eu, respectively. Samples were subsequently sonicated for about 1 min, and then air-dried upon deposition onto glass slides. Diffraction patterns were collected using a Rigaku Ultima III Diffractometer, operating in the Bragg configuration using Cu Kα radiation (1.54 Å), and spanning a range from 20 to 60° measured at a scanning rate of 1° per minute.

2.2.2. Electron microscopy

SEM images were obtained at 10 kV on a JEOL 7600F instrument. Low-magnification TEM images were taken at an accelerating voltage of 120 kV on a JEOL JEM-1400 instrument, equipped with EDS mapping capabilities. HRTEM images coupled with the ability to obtain selected area electron diffraction (SAED) patterns were recorded using a JEOL JEM-3000F microscope equipped with a Gatan image filter (GIF) spectrometer operating at an accelerating voltage of 300 kV. Specimens for all of these microscopy experiments were prepared by dispersing the as-prepared product in ethanol, sonicating for 2 min to ensure an adequate dispersion of the nanostructures, and dipping one drop of the solution onto a Si wafer for SEM and a 300 mesh Cu grid, coated with a lacey carbon film, for TEM and HRTEM analysis.

2.2.3. FTIR

FTIR spectra were collected on a Nexus 670 instrument (ThermoNicolet) equipped with a Smart Orbit diamond ATR accessory, a KBr beam splitter, and a DTGS KBr detector. As-prepared solid powder samples were placed onto the crystal surface, where data were taken with a reproducible pressure. A background correction in air was performed in the spectral range studied. FTIR data were typically recorded over the wavenumber range of 1000–4000 cm^{-1} and were subsequently evaluated in terms of expected, characteristic absorption bands. Spectra were recorded using the Omnic software with a spatial resolution of 1 cm^{-1}.

2.2.4. UV-visible and fluorescence spectroscopy

UV-visible spectra were collected at high resolution on a ThermoSpectronics UV1 spectrometer using quartz cells possessing a 10-mm path length. Spectra were obtained for CdSe QDs, $LaPO_4$: Eu 1D nanowires, $LaPO_4$: Eu 3D urchin-like architectures, and associated heterostructures, all of which were individually sonicated for 2 min so as to yield a homogeneous dispersion. Samples for PL spectra were dispersed in MeOH for AET-capped CdSe QDs as well as for CdSe QD –$LaPO_4$: Re (Re = Eu, Ce, and Tb) heterostructures. All of these were sonicated for 1 minute, prior to measurement. Fluorescence data were subsequently obtained at room temperature using a FluoroMax-4 spectrofluorimeter (Jobin Yvon) with 15 s and 5 s integration times, using excitation wavelengths of 260 nm and 380 nm, respectively. The corresponding fluorescence lifetimes were measured with a FluoroMax-4 spectrofluorimeter equipped with an IBH NanoLED, emitting at 388 nm as an excitation source, and a NanoLED controller module, Fluorohub (Jobin Yvon), operating at 1 MHz. Decay data analysis was characterized using the DAS6 software (Horiba Jobin Yvon IBH).

3. Results and Discussion

3.1. Structural Insights into 1D and 3D $LaPO_4$: Eu structures

The XRD patterns of our CdSe QDs (Figure S1) can be reliably assigned to the reflection of a crystalline hexagonal würtzite structure (JCPDS # 08-0459).[28] The corresponding purity and crystallinity of the 1D nanowire and 3D architectural motifs of $LaPO_4$: Eu were initially characterized using XRD. As shown in Figure 1, the XRD patterns of these samples suggest that the as-synthesized nanomaterials are composed of a single hexagonal phase, possessing a space group of P6222, which agrees well with the JCPDS #46-1439 database standard. The hexagonal phase of the $LaPO_4$ structure, which represents the prototype of both cerium and neodymium phosphates, consists of columns, built up of alternating lanthanum and phosphate ions, extending along the *c*-axis (open channel) of the hexagonal unit cell.[48] Due to the open channel configuration and the relatively long distance to the nearest oxygen neighbor within the structure, the material inherently contains a comparatively low density of the hexagonal isomorph, suggesting that the crystal structures can be stabilized overall by the presence of water molecules at the interstices at (0, 0, ½), (0, 0, 5/6), and (0, 0, 1/6), along the open *c*-axis channel.[48]

Indeed, the incidence of intercalated water molecules in the $LaPO_4$ structures has been readily confirmed by FTIR spectra, as illustrated in Figure S2. Notable peaks near 3420 cm^{-1} and 1632 cm^{-1} can likely be attributed to the bending and stretching vibrational modes of water molecules, and broad bands near 1064 cm^{-1} are associated with the PO_4^{3-} group in $LaPO_4$ structures.[49] The appearance of distinctive bands in Figure S2 is typical for the hydrated form of $LaPO_4$, as suggested by Hazel et al.[49] Furthermore, the transmittance IR intensity of water molecules (i.e. O-H stretching and bending vibrational modes) decreases with increasing annealing temperature, but is not noticeably dependent upon the morphology of 1D and 3D

structures, as shown in Figure S2. It has been implied that the number of water molecules in the structure is not significantly affected by the morphology of the structures (i.e. 1D nanowire versus 3D architectures) but is a smaller quantity for samples annealed at higher temperatures, consistent with the observation from previous studies of various other phosphate structures.[50] We note however that the presence of water molecules associated with the hexagonal phosphate structure does not appear to significantly affect their luminescent properties.[29]

3.2. Size, structure, and morphology of 1D and 3D $LaPO_4$: Eu nanostructures

The size, structure, and morphology of 1D and 3D structural motifs of $LaPO_4$: Eu have been investigated using TEM. Typical TEM images of 1D $LaPO_4$: Eu nanowires are shown in Figure 2A and C. Specifically, Figure 2C corresponds to a higher magnification image of 1D $LaPO_4$: Eu nanowires. On the basis of statistical measurements of several tens of nanowires pertaining to each of our samples, our as-prepared $LaPO_4$: Eu nanowires measure on average 7.3 ± 0.52 nm in diameter with lengths of up to 1.1 ± 0.21 μm. The observed nanowire formation is not surprising, considering that the crystal structure of hexagonal $LaPO_4$ consists of infinite linear chains of alternating lanthanum and phosphate ions, extending along the *c*-axis. From a thermodynamic perspective, the intermolecular bonding between these chains is considerably weaker than the intramolecular bonding within the chains themselves, such that the activation energy for the *c*-axis direction of growth for hexagonal $LaPO_4$ is lower than that for a corresponding growth direction, perpendicular to the *c*-axis itself.[39, 48] Hence, both the crystal structure and thermodynamic data collectively support the idea of a higher growth rate along the *c*-axis, thereby favoring the relatively facile formation of $LaPO_4$ nanowires.

Figure 2B and D display typical TEM images of 3D architectures of $LaPO_4$: Eu at both lower and higher magnifications, respectively. Each relatively uniform 3D structure possessing a

diameter of ~500 nm (i.e. average diameter of 475 ± 40 nm, based on statistical measurements of tens of 3D architectures synthesized using optimized protocols) is composed of a very high density of numerous constituent nanowires pointing outwards in a radial manner. The inherent size monodispersity and shape uniformity of our 3D $LaPO_4$: Eu architectures at the sub-micron scale are further confirmed by additional low magnification SEM images (Figure S3).

3.3. Growth mechanism of 3D $LaPO_4$: Eu urchin-like architectures

In order to examine and understand the reaction conditions associated with the formation of 3D urchin-like architectures of $LaPO_4$: Eu, in Figure 3, we probed using SEM the evolution of the growth of the hierarchical crystal morphology as a function of (i) reaction time as well as of (ii) the nominal precursor La/P ratio, an indirect measure of the chemical potential. In a typical procedure, the spherical 3D structure appears to have been generated essentially immediately upon the addition of H_3PO_4, in a manner independent of the chemical potential, throughout the range of molar elemental ratios of La/P spanning from 0.5 to 1 (Figure 3 A, D, and G), suggesting that the nucleation and growth processes associated with the formation of 3D structures are reasonably fast. Nonetheless, the actual sizes of the 3D structures are strongly affected by both the La/P molar elemental ratio as well as the growth time.

Specifically, these sizes correlate proportionately with higher La/P molar elemental ratios (i.e. chemical potential) and longer reaction times. For example, the size distribution for 3D structures more than doubles from 485 ± 75 nm for samples initially prepared at 0 h with a molar elemental ratio of La/P = 0.5 (Figure 3A) to 1.2 μm ± 350 nm for samples initially generated at 0 h, using a molar elemental ratio of La/P = 1 (Figure 3G). Moreover, during the reaction time interval analyzed from 0 h to 4 h, the corresponding size distributions of the 3D architectures of $LaPO_4$: Eu also gradually increase from 485 ± 75 nm for samples synthesized at 0 h using a

molar elemental ratio of La/P = 0.5 (Figure 3A) to 980 ± 130 nm for samples created after 4 h of reaction time with an identical molar elemental ratio of La/P = 0.5 (Figure 3C). All of these values were obtained, based on the statistical measurements of tens of various discrete, individual 3D-like architectures, as visualized by SEM.

What ideas can potentially explain these data? As a reasonable postulate, faster 3D growth is presumably associated with the corresponding faster growth rate of its constituent component 1D $LaPO_4$: Eu nanowires at higher chemical potentials, a concept consistent with the model suggested by Peng et al.,[51, 52] wherein one-dimensional growth is favored in solution under similar reaction conditions. Therefore, to gain additional insights and to investigate the growth mechanism of our 3D $LaPO_4$: Eu sub-micron scale spherical architectures in more detail, the corresponding time-dependent evolution (t = 0 h, 1 h, 2 h, 4 h, and 6 h, respectively) of the 3D hierarchical crystal morphology at a constant La/P molar ratio of 0.5 in the presence of an excess of MHA molecules (i.e. molar ratio of MHA/La = 9) was recorded using SEM (Figure 4).

These reaction conditions were chosen, since an excess of carboxylic acid-terminated MHA moieties can relatively and easily form a stable complex with La in the form of La^{3+} $-(COO^-)_3$, which can potentially slow down the nucleation process as well as the subsequent growth of the precursor intermediates. In accordance with LaMer's model,[53] the formation of such metal-based complexes functionally isolates and traps La ions, thereby lowering the effective concentration of free La ions in solution. In so doing, such a chemical strategy can help in modulating (i.e. reducing) the corresponding nucleation and growth rates of as-prepared phosphate crystals.[54] A similar explanation has also been put forward to explain how the presence of metal-(COO^-) complexes can control the production of 3D hierarchical structures of metal oxides including but not limited to $CePO_4$,[43] $CaMoO_4$,[55] $NaY(MoO_4)_2$,[46] and $NiCo_2O_4$.[56]

Immediately after the addition of H_3PO_4, the as-obtained structural morphology of $LaPO_4$: Eu consists of 1D nanowire building blocks (Figure 4A), and some of these individual nanowires presumably aggregate over time in a self-assembled manner, in the presence of MHA. Furthermore, the discrete nanowires become somewhat more aggregated, and the aggregates themselves gradually become larger, as the corresponding reaction time increases (Figure 4B and C). In fact, based upon statistical measurements of tens of individual, discrete 3D motifs as evident from SEM analysis, the average aggregate diameter noted is 110 nm ± 96 nm after 1 h of reaction (Figure 4B) and 173 nm ± 155 nm after 2h of reaction (Figure 4C). As the reaction time attained a value of 4 h (Figure 4D), larger, more uniform, and better well-defined 3D nearly spherical, 'ball-like' architectures were obtained, measuring 950 ± 108 nm in diameter, though some smaller aggregates still remained. After finally 6 h of reaction time (Figure 4E), relatively larger (average diameter of 1.23 μm ± 150 nm) distinctive 3D urchin-like architectures of $LaPO_4$: Eu were apparent.

As a control experiment, we should note that Figure 4F represents a typical SEM image of $LaPO_4$ prepared by the same protocol in the absence of MHA. Clearly, as-obtained $LaPO_4$ generated without MHA mainly consists of a collection of 1D nanowire motifs, and although some of these 1D nanowires are aggregated, these clusters do not resemble urchin-like assemblies at all, thereby implying that the presence of MHA itself inherently plays a crucial role in determining the specific formation of 3D urchin-like morphologies of $LaPO_4$.

Hence, on the basis of these time-dependent experimental results, we can propose a possible, plausible mechanism for the formation of 3D motifs of $LaPO_4$: Eu. Initially, in aqueous solution, the terminal COO- pendant moiety within MHA reacts with La^{3+}, so as to generate $La^{3+} – (COO^-)_3$ complexes, which are observed as white flocculates, immediately after the addition of

MHA to dissolved La ions (Figure 5A). After the addition of H_3PO_4 in the solution, nucleation events presumably occur (Figure 4A and Figure 5B). Subsequently, 'fragmentary' growth begins by Ostwald ripening along the uniaxial direction, due to the intrinsic anisotropic crystalline structure of $LaPO_4$. Although the $La^{3+} - (COO^-)_3$ complexes are somewhat destroyed by the presence of PO_4^{3-} and the subsequent formation of small presumably amorphous seed nuclei of $LaPO_4$, MHA molecules can still attach themselves onto the surfaces of $LaPO_4$ nuclei through favorable electrostatic interactions (Figure 5B). Nonetheless, as discussed earlier, the presence of complexes of $La^{3+} -(COO^-)_3$ can presumably slow down the nucleation and subsequent anisotropic linear growth of $LaPO_4$, thereby resulting in the formation of either shorter lengths of nanowires or smaller nanowire aggregates (measuring < 1 μm) as compared with nanowires prepared in the absence of MHA (measuring > 2 μm, as shown in Figure 4F). In any event, these smaller primary 'precursor' $LaPO_4$ nanowires can subsequently attach together in an oriented manner, and spontaneously aggregate into more stable, self-assembled, crystalline 3D urchin-like architectures (with the wire-like crystallites radiating outwardly from an inner core), so as to minimize surface energy in the presence of MHA (Figure 4B and 4C, as well as Figure 5D).

We should note that MHA has already been extensively used in the formation of self-assembled monolayers of Au nanoparticles into urchin-like assemblages.[57-59] MHA is a chemically interesting 'ligand' molecule, in that it is terminated not only with carboxylic acid molecules, which are readily soluble in water, but also with thiol species, which are inherently less soluble in aqueous solution due to its inability to easily hydrogen bond. Moreover, thiols can be readily oxidized to disulfides (which are also insoluble in water) by unreacted H_3PO_4. In fact, we note that 3D architectures of $LaPO_4$: Eu can be more easily formed in the presence of an

excess of H_3PO_4 (i.e. lower La/P ratios), as shown in Figure 3A-I, as compared with reaction using a higher La/P molar elemental ratio of 1.5 (Figure S4).

One hypothesis to explain this observation is that insoluble disulfides generated by unreacted H_3PO_4 can facilitate the formation of 3D urchin-like architectures of $LaPO_4$ due to the greater relative solubility and polarity differential between exposed disulfide moieties versus thiols in the presence of water. Thus, according to this theme, $LaPO_4$ nanowires are more likely to aggregate and self assemble to form more complex 3D micelle-like structures in order to sequester, isolate, and confine the water-insoluble disulfide/thiol regions within a central hydrophobic core. In Figure 5D, the idea of forming a 'micellar' structure, possessing exposed 'solvent-friendly' outer hydrophilic moieties protecting a less hydrophilic inner region, is implicitly implied. Nonetheless, the assembled nanowires can still undergo a Ostwald ripening process in a radial direction, thereby forming the observed urchin-like 3D structures of $LaPO_4$ (Figure 4D and E and Figure 5E).

We also attempted similar reactions in the presence of either 3-mercaptopropioic acid (MPA) or 11-mercaptoundecanoic acid (MUA), which are similar to MHA. Indeed, these molecules consist of identical end groups but with different alkyl chain lengths. We found that the average sizes and morphologies, respectively, of the resulting 3D structures prepared with the use of MPA are not only smaller but also more irregular as compared with MHA. Moreover, the size distributions of the aggregates measured was correspondingly much broader (i.e. from 100 nm to 1 μm) (Figure S5A). By contrast, with the use of MUA, the as-obtained $LaPO_4$: Eu morphology consisted primarily of 1D nanowire aggregates; no 3D clusters formed (Figure S5B). Hence, the use of MHA as an 'optimal' surfactant can apparently isolate, homogenize, and disperse crystalline precursor seeds in a manner, favoring the formation of more regular 3D

hierarchical structures. Synthetic optimization as well as an investigation of the precise role of the chain length of MHA versus MPA and MUA in terms of correlating 'surfactant' chemical structure with the as-generated motifs of $LaPO_4$: Eu will likely be the focus of future studies.

Interestingly, in our work, the sizes of our 3D structures of $LaPO_4$ are in the sub-micron range, which is considerably smaller than analogous structures (measuring over 3 μm in general), associated with various phosphates, vanadates, and tungstates, which have been mainly prepared using hydrothermal methods.[36, 43-45] One explanation for the significantly smaller sizes of our as-prepared 3D $LaPO_4$ materials as compared with other reports may be attributed to the correspondingly shorter chain lengths of the 'surfactant' we used (i.e. MHA) as compared with dioctyl sodium sulfosuccinate and cetyl tri-ammonium bromide, which are typically utilized in the formation of 3D structures of these various other analogous materials.[43, 60, 61] That is, the sizes of our 'micelle-like' structures, forming the basis of our 3D complex urchin-like materials herein, are likely smaller as compared with analogous species for other hierarchical materials, because of our use of inherently smaller 'surfactant' molecules.[62, 63] Collectively, our results demonstrate the feasibility of 'nanomanufacturing', i.e. a synthetic protocol predicated upon an ambient, simple, and solution-based methodology for the effective large-scale production of rare earth activated 3D urchin-like $LaPO_4$ architectures.

3.4. Structural Insights into CdSe QD - 1D and 3D $LaPO_4$: Eu heterostructures

Electron Microscopy. Figure 6 A and D highlight typical TEM images associated with the formation of CdSe QD-$LaPO_4$: Eu 1D nanowires and CdSe QD - $LaPO_4$: Eu 3D urchin-like heterostructures, respectively. Although complications associated not only with the lack of contrast variation between CdSe QDs and $LaPO_4$: Eu but also with the presence of aggregation of nanowires and QDs prevented a clear differentiation between the two different nanostructures,

we were nonetheless able to discern distinctive regions wherein CdSe QDs were anchored onto both the 1D and 3D $LaPO_4$: Eu structures, as highlighted by the yellow circles in Figure 6A and D, respectively. Moreover, the HRTEM images (Figure 6 B and E) of individual CdSe QD - $LaPO_4$: Eu heterostructures clearly suggest that highly crystalline CdSe QDs are indeed adjacent to and closely bound onto the underlying 'template supports' of $LaPO_4$: Eu 1D nanowires and 3D sub-micron structures. In addition, HRTEM revealed interlayer spacings, corresponding to the expected lattice parameters associated with the hexagonal crystal structure of $LaPO_4$: Eu and CdSe QDs, respectively. Specifically, (i) 0.215 nm and 0.34 nm were in good agreement with the expected *d* spacings for the (200) and (110) lattice planes of QDs and $LaPO_4$, respectively, within the 1D nanowire-based heterostructures, whereas (ii) 0.215 nm and 0.217 nm for the (211) and (110) planes of the 3D heterostructures were consistent with the expected lattice planes for QDs and $LaPO_4$, respectively, within the 3D urchin-based heterostructures. The associated SAED pattern (Figure 6C and F) revealed disordered diffraction spots, which might have originated from the overall polycrystallinity of the structures. Particular features though within the individual discrete diffraction patterns could be specifically assigned either to CdSe QDs or to $LaPO_4$: Eu nanostructures (1D and 3D), as indicated in Figure 6C and F, respectively.

From the standard TEM data, aggregation and contrast issues rendered it difficult to qualitatively and quantitatively determine either the degree of spatial localization or the extent of coverage of QDs on the underlying 1D and 3D $LaPO_4$: Eu structures. Hence, a detailed chemical analysis was carried out using energy-dispersive X-ray spectroscopy (EDS) in order to probe elemental composition throughout the heterostructures, so as to confirm the presence of CdSe QDs immobilized not only on the outer surfaces of 1D nanowires but also throughout the

expansive volume and surface area (i.e. inner and outer surfaces and edges) of the corresponding 3D $LaPO_4$: Eu structures.

Specifically, STEM images of typical 1D nanowires and 3D urchin-like structures as well as their corresponding elemental maps are highlighted in Figure 7A-F and Figure 8A-F, respectively, and these data shed light on the spatial distributions of the constituent elements, i.e. La, P, O, Cd, and Se. Importantly, in Figure 7 and 8E and F, the locations of the Cd *L*-edge and the Se *K*-edge signals overlap and coincide reasonably well with those of the La *L*-edge, the O *K*-edge, and the P *K*-edge signals (Figure 7 and 8B, C, and D), thereby indicating that CdSe QDs are likely attached to and spatially distributed throughout the external surfaces of both $LaPO_4$: Eu 1D nanowires and 3D urchin-like architectures. However, the intensity of the signal distribution associated with the Cd *L*-edge and Se *K*-edge within the 1D nanowire-based heterostructure is significantly lower than that of the corresponding 3D urchin-like heterostructures, thereby implying that CdSe QD-1D $LaPO_4$: Eu heterostructures likely maintain overall lower quantities of bound CdSe QDs as compared with their CdSe QD-3D $LaPO_4$: Eu counterparts.

In order to further confirm and corroborate the qualitative coverage density by EDS mapping (Figure S6A and B), a more rigorous quantitative analysis to determine the coverage density of CdSe QDs on both 1D and 3D-based $LaPO_4$: Eu structures was performed with the use of the obtained weight % (wt %) values for both $LaPO_4$ structures as well as of Cd and Se atoms within the heterostructures, as determined from the EDS spectral and mapping data.

We describe our detailed reasoning and the mathematical protocol used to obtain our coverage values more extensively in the related Supporting Information section. From the results of our analysis, upon normalization to identical volumes (i.e. 10^6 nm^3) of 1D and 3D structures, we calculated that approximately 1200 QDs were attached onto 3D $LaPO_4$ urchin-like structures,

whereas only about 370 QDs were immobilized onto analogous 1D $LaPO_4$ nanowires under comparable reaction conditions, thereby suggesting that the numbers of CdSe QDs are likely to be nearly 3 times greater on the outer surfaces of 3D structures as compared with their 1D nanowire counterparts. The higher coverage density of CdSe QDs on complex 3D urchin-like structures versus 1D nanowires can be mainly ascribed to the higher exposed surface areas of 3D urchin-like structures as compared with either 1D nanowires, 1D nanorods, or 0D nanoparticles. Our results are consistent with similar observations for 3D hierarchical structures of various other inorganic systems, such as TiO_2, ZnO, Fe_2O_3, $CaMoO_4$, MnO_2, and $NiCo_2O_4$.[55, 64-67]

IR Spectroscopy. The actual surface chemical bonding of the heterostructures has been confirmed by FTIR spectra. Specifically, Figure 9 highlights the FT-IR spectra of 3D $LaPO_4$: Eu, CdSe QD-3D $LaPO_4$: Eu heterostructures, and AET-capped CdSe QDs, respectively. For the latter two QD-derived materials, the presence of bands associated with N-H stretching vibrations has been monitored near 3232 cm^{-1}. Additional distinctive peaks near ~1585 cm^{-1}, in the region of 900-1100 cm^{-1}, and at 713 cm^{-1} have been ascribed to the N-H bending, C-N stretching, and N-H wagging vibrational modes, respectively, of ligand-derived, primary amine molecules bound onto QDs in the form of AET-capped CdSe QDs.[68] The absence of an S-H band near 2550-2600 cm^{-1} in these spectra confirmed that the AET ligands were likely immobilized onto CdSe QDs. Notable peaks near 3410 cm^{-1} and 1630 cm^{-1} can likely be attributed to stretching and bending vibrational modes of water molecules, respectively, with broad bands located near 1064 cm^{-1}, ascribed to the PO_4^{3-} group in 3D $LaPO_4$ urchin-like architectures.

In the corresponding CdSe QD – $LaPO_4$: Eu heterostructures, the IR spectra contain a number of specific peaks, which are clearly altered in position and intensity as compared with those associated with single, individual CdSe QDs and $LaPO_4$: Eu 3D urchin-like structures.

First, the expected N-H wagging vibration near 713 cm^{-1}, assigned to AET ligands bound onto as-prepared CdSe QDs, is blue-shifted to 731 cm^{-1} within the heterostructures. Second, the water-based O-H stretching vibrational band near 3410 cm^{-1} is shifted to 3450 cm^{-1}.

These data imply that the presence of intermolecular hydrogen bonding (i.e. through the presence of N-H---O-H or H-N---H-O linkages) is likely associated with the formation of AET-capped CdSe QD–$LaPO_4$: Eu heterostructures.[69, 70] However, the intensity of the expected ligand-derived N-H stretching vibration in AET-capped CdSe QDs near 3232 cm^{-1} decreases within the heterostructure motif itself and overlaps with the broad O-H stretching mode, rendering it difficult to observe an expected IR peak shift in the position of the N-H band. We do note that the positions of the relatively weak O-H and N-H bending vibrations near 1630 and 1585 cm^{-1} are still apparent, but are not significantly shifted in position in the heterostructures. Comparable overall IR behavior was noted for both 1D and 3D heterostructures, and the optical signatures of the 1D composites and those of the individual component subunits are highlighted in Figure S7.

3.5. Optical data on AET-capped CdSe QD-1D and 3D $LaPO_4$: Eu heterostructures

UV-visible absorption spectra of as-prepared CdSe QDs, $LaPO_4$: Eu, and the resulting heterostructures are shown in Figure S8. Specifically, CdSe QDs and $LaPO_4$: Eu nanowires exhibit pronounced absorption peaks in the regions of 380-600 nm and ~250-290 nm, respectively, as expected. No significant differences between the absorbance intensity of CdSe QDs and of CdSe QD – 3D $LaPO_4$: Eu heterostructures were observed near the first excitonic absorption peak near 565 nm, suggesting that the overall optical densities of CdSe QDs and of the corresponding CdSe QD – 3D $LaPO_4$: Eu heterostructures are likely comparable. However, the absorbance profile of CdSe QDs in CdSe QD – 1D $LaPO_4$: Eu heterostructures possesses less

sub-structure as compared with that of the 3D $LaPO_4$: Eu-based heterostructures. One explanation for that observation is that the concentration and therefore the corresponding coverage of CdSe QDs in the final, resulting CdSe QD–1D $LaPO_4$: Eu heterostructures are less than that in analogous CdSe QD-3D $LaPO_4$: Eu heterostructures, an assertion which would be consistent with as-obtained EDS mapping results, shown in Figures 7 and 8.

Steady-state PL spectra of AET-capped CdSe QDs and of the analogous AET-capped CdSe QD - $LaPO_4$: Eu 1D and 3D heterostructures excited at 380 nm (3.26 eV) are shown in Figure 10A and B. Specifically, the emission spectrum of CdSe QDs consists of a high-energy peak, corresponding to a band edge emission at 580 nm without any evident surface trap emission in the near infrared region, thereby implying that the CdSe QDs are likely to be uniformly and densely capped with AET ligands. However, at 380 nm excitation, because the absorption intensity of $LaPO_4$: Eu within the heterostructures is significantly lower, as shown in the absorption spectra in Figure S8, it was likely that the distinctive spectral feature of $LaPO_4$: Eu was most likely overwhelmed by the emission peak profile of CdSe itself. In effect, we only observed two small shoulders in the spectrum of the 1D and 3D $LaPO_4$-based nanoscale composites, which could be ascribed to the *f-f* transitions ($^5D_0$-$^7F_2$ and $^5D_0$-$^7F_4$) of Eu^{3+}-doped $LaPO_4$ (Figure S9). By contrast, upon excitation at 260 nm, the spectral features of $LaPO_4$: Eu were more evident and visible; that is, the characteristic emission bands of Eu^{3+} at 492, 547, 589, and 623 nm could be ascribed to the *f-f* transitions, emanating from corresponding transitions in the $^5D_0$-$^7F_1$, $^5D_0$-$^7F_2$, $^5D_0$-$^7F_3$, and $^5D_0$-$^7F_4$ levels, respectively, as shown in Figure 10C and D.

In general, to explain the optical behavior of heterostructures, two potential pathways, highlighting external non-radiative relaxation pathways of photogenerated excitons, should be considered. These include (i) resonance energy transfer of both charge carriers and (ii) charge

transfer of one charge carrier, denoting processes which at times can operate simultaneously as shown by the arrows in Figure 10. From our data, what is obvious is that the PL intensities of the constituent precursor nanoscale 'building blocks', i.e. the AET-capped CdSe QDs as well as those of both 1D and 3D $LaPO_4$: Eu, are substantially reduced within the final discrete composite structure itself. Herein, we suggest that the charge transfer from the CdSe QDs to $LaPO_4$: Eu represents a dominant relaxation pathway, leading to PL quenching of CdSe QDs, whereas the observed PL quenching of $LaPO_4$: Eu can mainly be attributed to energy transfer occurring from $LaPO_4$:Eu to CdSe QDs.

3.5.1. Evidence for Charge transfer in Heterostructures

Specifically, we postulate that the PL quenching observed for the CdSe QDs within the heterostructure can be attributed to charge transfer from photo-excited CdSe QDs to $LaPO_4$: Eu through the mediation of water molecules intercalated within the $LaPO_4$ structure. Our observation is consistent with data from prior reported literature.[71] In particular, Pechstedt et al.[71] studied the critical effect of water molecules on the corresponding PL intensity of colloidal CdSe/ZnS QDs and noted that the quantum yield of QDs decreased with increasing amounts of and increasing exposure times to water molecules, likely as a result of photo-generated charge transfer from the QDs to water itself.

Furthermore, we found that the PL intensity of our AET-capped CdSe QDs is substantially quenched even within AET-capped CdSe QD - undoped $LaPO_4$ 1D and 3D heterostructures, as shown in Figure 10A and B. This was a curious result, because $LaPO_4$ possesses a wide band gap (~8 eV). Moreover, the difference between the intrinsic conduction and valence band energy levels of $LaPO_4$ exceeds in magnitude and extends beyond that of the CdSe QDs themselves,[72] a scenario which does not represent an ideal condition for the presence

of charge transfer from CdSe QDs to $LaPO_4$ in terms of favorable energy level alignment. Hence, the observation of a decreased PL intensity of CdSe QDs within the context of CdSe QD-undoped $LaPO_4$ heterostructures is consistent with the idea that the PL quenching of our CdSe QDs is connected to photo-induced interactions with the intercalated water molecules associated with the $LaPO_4$ structure.

To further probe the nature of the interactions between CdSe QDs and the adjoining 1D and 3D $LaPO_4$: Eu nanoscale structures, we monitored the emission decay behavior, obtained using a 388 nm laser pulse as the excitation source. Figure 11 highlights the resulting excitonic emission decay of CdSe QD-$LaPO_4$: Eu 1D and 3D-based heterostructures. Specifically, the emission decay evinced multi-exponential behavior, because the distribution of the recombination rate constants associated with this complex architecture likely influenced the resulting decay kinetics.[73] Indeed, tri-exponential decay kinetics could be used to determine the corresponding emission lifetimes. The overall trends observed are consistent with the steady-state PL emission spectra (Figure 10). That is, AET-capped CdSe QDs evinced an initial average lifetime (τ_{av} = 7.3 ns) that decreased in magnitude when these functionalized dots were incorporated as part of either CdSe QD - $LaPO_4$: Eu 1D or 3D-based heterostructures, likely as a result of charge transfer occurring from CdSe QDs to water molecules in $LaPO_4$: Eu.

3.5.2. Evidence for Energy transfer in Heterostructures

As observed in Figure 10A and B, upon excitation at 380 nm, the PL emission of AET-capped CdSe QDs in CdSe: Eu activated $LaPO_4$-based composites is higher than that as compared with the corresponding control samples of AET-capped CdSe QD – undoped $LaPO_4$ 1D and 3D-based heterostructures. Such an enhancement of the PL intensity of CdSe QDs in the presence of the Eu dopant can potentially be ascribed to energy transfer from $LaPO_4$: Eu

nanostructures to CdSe QDs. This idea is reasonable, because the spectral overlap between the emission band of the energy donor ($LaPO_4$: Eu) and the absorption band of energy acceptor (CdSe QDs) is substantial, as shown in Figure 12D, and it represents one of the critical conditions for energy transfer. Furthermore, as noted by others,[23, 65] it is known that CdSe QDs can be a reasonable acceptor for energy transfer in the presence of inorganic and organic rare earth doped compounds.[27, 74] To additionally highlight the plausibility of energy transfer occurring between QDs and attached species, other groups have noted an enhancement of the visible excitation bands of Eu^{3+} or Ce^{3+} likely as a result of energy transfer taking place from CdTe QDs to proximal YVO_4: Eu^{3+} and $CePO_4$, respectively.[75, 76]

Coupled with the PL enhancement of CdSe QDs in Eu-doped $LaPO_4$–based heterostructures as compared with their undoped analogues, we also observed a corresponding PL quenching of Eu activated $LaPO_4$ itself upon binding of $LaPO_4$: Eu to CdSe QDs upon excitation at 260 nm and at 380 nm, respectively (i.e. Figure 10C and D and Figure S9). Overall, these data suggest and imply a degree of energy transfer from Eu-activated $LaPO_4$ to AET-capped CdSe QDs, thereby decreasing the PL signal of $LaPO_4$: Eu and enhancing the corresponding relative PL signature of the CdSe QDs.

We can model this process as follows. Assuming that the PL quenching of Eu activated $LaPO_4$ can be completely attributed to energy transfer to CdSe QDs, the corresponding energy-transfer efficiency (η_T) can be expressed by:[77]

$$\eta_T = 1 - \frac{I_s}{I_{so}} \qquad (1)$$

where I_{SO} and I_S denote the peak intensities of Eu-activated $LaPO_4$ both in the absence and presence of CdSe QDs, respectively. As a consequence, the calculated η_T values for 3D and 1D Eu $LaPO_4$ attached onto CdSe QDs were computed to be 55% and 44%, respectively, using the

same optimized CdSe concentration for both heterostructures. These data are comparable to a previous report concerning the efficiency of energy transfer from CdTe QDs to Eu-activated YVO_4, wherein a value of ~50% was computed.[75] To further confirm the nature of the interactions between CdSe QDs and the adjoining 1D and 3D $LaPO_4$: Eu nanoscale structures, respectively, we noted that the average lifetime of AET-capped CdSe QDs attached to Eu-doped $LaPO_4$ was noticeably longer than that of comparable QDs linked with undoped $LaPO_4$, an observation likely arising as a consequence of intramolecular energy transfer taking place within the heterostructure itself from $LaPO_4$: Eu to the bound CdSe QDs (Figure 11).

Nonetheless, the emission ranges of both AET- capped CdSe QDs and $LaPO_4$: Eu are close to the detection limit of our PL spectroscopy instrument, under 260 nm and 380 nm excitation, respectively. Hence, the acquisition of reliable quantum yield (QY) values and lifetimes of the $LaPO_4$: Eu itself within the resulting heterostructures is beyond the scope of the current study. Therefore, with the use of highly sophisticated optical spectroscopic methods, in the future, we will be able to measure QY and the lifetime variation of Eu-activated $LaPO_4$ within our heterostructures, and thereby quantify the relative optical contributions of charge and energy transfer within our heterostructures.

3.5.3. Effect of Morphology: Optical behavior of CdSe QDs attached to 1D vs. 3D $LaPO_4$: Eu

Interestingly, the extent of the PL quenching behavior of CdSe QDs with 3D-based heterostructures is different from that for the corresponding 1D-based heterostructures, as shown in Figure 10A and B, thereby indicating that the efficiency of charge and energy transfer from CdSe QDs to $LaPO_4$: Eu and vice versa is significantly affected by the precursor morphology of $LaPO_4$: Eu itself. As we discussed earlier, based on TEM and EDS mapping data, nearly 3 times as many CdSe QDs are anchored onto 3D $LaPO_4$: Eu urchin-like structures as compared with

their 1D $LaPO_4$: Eu nanowire counterparts. Hence, it is reasonable to assume that the corresponding magnitudes of the optical interactions (e.g. the intrinsic charge and energy transfer processes themselves) between CdSe QDs and 3D $LaPO_4$: Eu urchin-like structures are considerably more pronounced by analogy with their 1D nanowire counterparts.

In terms of actual data, the normalized PL intensity of AET-capped CdSe QDs is substantially decreased when coupled with undoped 3D $LaPO_4$ urchin-like materials as compared with undoped 1D $LaPO_4$ nanowires, thereby indicating that better charge transfer through the mediation of water molecules in $LaPO_4$ can be achieved in CdSe QD-3D urchin-like $LaPO_4$ heterostructures as compared with their 1D analogues (Figure 10A and B). In addition, a greater and more pronounced PL enhancement of CdSe QDs in Eu-activated 3D urchin-like heterostructures has been calculated to occur with a higher energy transfer efficiency ($\eta_T \sim 55\%$) as compared with their 1D composite analogues ($\eta_T \sim 44\%$).

We attribute this observation to an improved energy transfer process from Eu within doped $LaPO_4$ to CdSe QDs. As additional evidence, more significant PL quenching of 3D $LaPO_4$: Eu as compared with 1D $LaPO_4$: Eu (Figure 10C and D) within the heterostructure motif further supports the notion of a more effectual energy transfer taking place from the 3D $LaPO_4$: Eu component to the CdSe QD unit, as compared with their 1D $LaPO_4$: Eu analogues. One explanation for this phenomenon is that the higher density, the higher concentration, as well as the spatially more uniform and more radial distribution of QDs localized throughout the entire volume of the 3D $LaPO_4$ motif enables a much more efficient CdSe QD absorption of the corresponding intrinsic luminescent $LaPO_4$: Eu emission.

As an added nuance, average lifetimes of 3D-based Eu^{3+}-doped heterostructures (τ_{av} = 5.1 ns) were longer than those of the corresponding 1D-based Eu^{3+}-doped heterostructures (τ_{av} = 3.2

ns). The longer lifetimes observed for 3D-based heterostructures as compared with their 1D-based analogues could again likely be attributed to greater efficiency of energy transfer from $LaPO_4$: Eu to CdSe QDs, because of the obviously larger quantity of anchored CdSe QDs onto the underlying 3D $LaPO_4$ surface as compared with 1D nanowires. Additional detailed parameters and equations used to obtain average lifetimes reported herein are described in Table S1 of the Supporting Information section.

We also note that the PL intensity of the unbound 1D $LaPO_4$: Eu itself is actually slightly higher than that of 3D $LaPO_4$. We can ascribe this observation to the fact that the inherent crystallite size of 1D $LaPO_4$: Eu (d = 14 nm, as estimated by the Debye-Scherrer formula), which intrinsically controls and is proportional to the quantum yield of rare-earth doped phosphors,[78, 79] is larger than that of the individual constituent components of polycrystalline 3D $LaPO_4$: Eu (d = 8 nm). These results are consistent with our prior XRD data (Figure 1).

Therefore, on the basis of all of these data, notably (i) the obvious excitonic emission quenching and (ii) the shortened lifetimes of CdSe QDs within the context of CdSe QD-$LaPO_4$: Eu nanoscale composite heterostructures, we can reasonably conclude that a photogenerated charge transfer mechanism represents a major relaxation pathway of CdSe QDs in CdSe QD-$LaPO_4$: Eu heterostructures. Conversely, the PL quenching of $LaPO_4$: Eu coupled with the relative PL enhancement of CdSe QDs in CdSe QD-$LaPO_4$: Eu heterostructures as compared with CdSe QD - undoped $LaPO_4$ heterostructure analogues indicates that energy transfer likely does occur to a large extent from $LaPO_4$: Eu to CdSe QDs. Not surprisingly then, despite the potential for relatively more efficient charge transfer occurring from CdSe QDs to $LaPO_4$ within 3D-based $LaPO_4$-based heterostructures because of the sheer abundance of intercalated water molecules, the CdSe QDs incorporated as part of 3D-based heterostructures actually exhibit less

PL quenching, as well as longer average lifetimes of CdSe QDs as compared with QDs in analogous 1D composites.

This evident dependence of optical behavior upon morphology can presumably be ascribed to a more effective energy transfer process taking place from 3D $LaPO_4$: Eu to CdSe QDs, which can be attributed not only to a higher QD coverage density but also to a correspondingly more efficient absorption of the emission of 3D $LaPO_4$: Eu, as compared with their 1D $LaPO_4$: Eu counterparts. In this light, the relative enhancement of PL of CdSe QDs can be specifically ascribed to energy transfer from $LaPO_4$: Eu to CdSe QDs in our heterostructures under UV excitation.

Such an effect could potentially enhance the practical applicability of QDs by not only improving their UV absorption behavior in the presence of $LaPO_4$: Eu but also generating more excitons in QDs with the possibility of higher QYs upon excitation at higher energies. We should note that it is well known that the exciton loss by non-radiative relaxation channels in QDs under higher energy excitation conditions (e.g. deep UV or X-ray) represents a limitation to the practical use of QDs within the context of light-sensitized, light-harvesting, or light-driven devices.[80] Thus, the creation of CdSe QD- $LaPO_4$: Eu 3D-urchin-like heterostructures constitutes the formation of a potentially novel class of hierarchical photovoltaic architectures with the capability for promoting highly efficient charge separation with longer observed lifetimes.

3.6. Effect of Dopant: Optical behavior of Heterostructures of AET-CdSe QDs attached to 3D $LaPO_4$: Re (Re = Ce, Tb, and Eu).

3.6.1. PL emission and lifetime analyses

As an additional, important reaction variable with which to control and correlate optical behavior, we systematically varied the nature of the rare earth dopant in our $LaPO_4$-based

heterostructures. Specifically, the optical properties of CdSe QDs and of the corresponding rare-earth doped $LaPO_4$ heterostructures are significantly dependent upon the nature of the various rare earth dopants, since the shape of the resulting emission spectra, the emission wavelength, and the associated luminescence mechanism are inherently determined by these dopant ions.

Figure 12A highlights the PL spectra of unbound AET-capped CdSe QDs, AET-capped CdSe QD – rare earth ion (i.e. Ce, Tb, and Eu) activated $LaPO_4$ -based 3D urchin-like structures, as well as a control sample of CdSe QD – undoped $LaPO_4$ 3D urchin-like heterostructures under 380 nm excitation. The observed PL quenching of CdSe QD emission in all of these heterostructures as compared with unbound CdSe QDs can presumably be attributed to charge transfer from CdSe QDs to the intercalated water molecules within the $LaPO_4$ structure.

However, the actual amount of PL quenching is necessarily dependent upon the rare earth dopant investigated and becomes more pronounced in order of AET-capped CdSe QD- $LaPO_4$: Ce (LP-Ce) > AET-capped CdSe QD - $LaPO_4$ (LP) > AET-capped CdSe QD - $LaPO_4$: Eu (LP-Eu) > AET-capped CdSe QD - $LaPO_4$: Tb (LP-Tb) - based 3D urchin-like heterostructures. Regarding the Eu and Tb data in particular, as implied earlier, it is likely that (i) the PL quenching of LP-Eu and LP-Tb (Figure 12B) within the CdSe QD-$LaPO_4$–based 3D urchin-like heterostructures coupled with (ii) the relative PL enhancement of CdSe QDs, as compared with QDs in undoped control heterostructures, provide reasonable evidence for energy transfer as the predominant mechanism taking place from the rare-earth doped $LaPO_4$ to the CdSe QDs.

Moreover, since the spectral overlap between the emission band of LP-Tb and the absorption band of CdSe QDs is considerably larger than that between LP-Eu and CdSe QDs (Figure 12D), not surprisingly, the PL intensity of CdSe QDs within AET-capped CdSe QD-LP-Tb heterostructures is noticeably higher than for the analogous CdSe QD-LP-Eu heterostructures.

We note that the η_T value associated with energy transfer from either Eu or Tb activated $LaPO_4$ to CdSe QDs was calculated from equation 1 and is computed to be 55% from Eu-activated $LaPO_4$ to CdSe QDs and 63% from $LaPO_4$: Tb to CdSe QDs, respectively, depending on the nature of the dopant, using the same optimized concentration of CdSe QDs attached onto the proximal $LaPO_4$ species.

With Ce doping, the situation is different. In Figure 12A, we actually observe greater PL quenching and a lower PL intensity of AET-capped CdSe QDs within CdSe QD-LP-Ce heterostructures as compared with similar QDs attached to heterostructure samples containing undoped LP species. It is implied therefore that the non-radiative relaxation pathway of photo-generated CdSe QD emission within CdSe QD-LP-Ce heterostructures is dominated by charge transfer processes, mediated not only through intercalated water molecules but also through the presence of (i) the Ce^{3+} activator in the $LaPO_4$ structure and (ii) corresponding energy level alignment between CdSe QDs and LP-Ce species, a conclusion which is consistent with our prior work involving analogous CdSe QD-$CePO_4$: Tb nanowire heterostructures.[28] That is, it is unlikely that energy transfer occurs from LP-Ce to CdSe QDs under 380 nm excitation, because the overall emission profile of LP-Ce (i.e. λ_{em} = 280-380 nm, Figure 12C), which is located at higher energies than the excitation wavelength (i.e. λ_{ex} = 380 nm), is noticeably less intense in magnitude as compared with its LP-Tb and LP-Eu counterparts (Figure 12D), respectively.

Moreover, the average lifetimes measured for these nanoscale composites is consistent with the PL quenching data (Figure 13) in that the heterostructures give rise to considerably shorter lifetimes as compared with unbound CdSe QDs (7.3 ns). In fact, the observed order of decreasing PL lifetimes correlates with increased PL quenching of the CdSe QD emission in the order of AET-capped CdSe QD-LP-Ce (1.8 ns) < AET-capped CdSe QD-LP (2.3 ns) < AET-

capped CdSe QD-LP-Eu (5.1 ns) < AET-capped CdSe QD-LP-Tb (5.7 ns) - based 3D urchin-like heterostructures. Additional detailed parameters and equations used to obtain average lifetimes reported herein are described in Table S1 of the Supporting Information section.

3.6.2. Insights into quenching mechanism

All of this behavior can be explained by reference to the energy levels of Ce^{3+}, Eu^{3+}, and Tb^{3+} ions in $LaPO_4$ in addition to the valence (VB) and conduction (CB) bands of CdSe QDs, collectively highlighted in Figure 14. Very recently, Dorebos semi-empirically studied and reported on the electronic level structure of $LaPO_4$ possessing lanthanide activators.[72] The electronic configuration of Ce^{3+} is the simplest with one electron in the 4*f*-shell. This ion absorbs and emits through the mediation of 4*f*-to-5*d* transitions, which exhibit a broad band emission, as shown in Figure 11C. The VB of LP-Ce structures (i.e. ~5.9 eV relative to the vacuum level) is situated above the corresponding VB of CdSe (i.e. -6.1 eV). We note that the VB of CdSe QDs is substantially lower than that of CdSe bulk, due to quantum confinement effects, and therefore speculate that there should be a correspondingly larger difference in energy between the VB of the CdSe QDs and that of LP-Ce as compared with the corresponding VB differential between bulk CdSe and LP-Ce.

Nevertheless, this overall energy configuration can induce PL quenching of the CdSe QD luminescence, due to charge transfer from CdSe not only to water molecules but also, as an additional viable pathway, to LP-Ce (mostly as a result of hole transfer due to the strong hole scavenging ability of AET ligands[16, 68]), upon excitation of CdSe QDs. Hence, the PL quenching in 3D-based heterostructures of AET-capped CdSe QD-LP-Ce is understandably more significant as compared with their corresponding AET-capped CdSe QD- undoped $LaPO_4$ analogues. That is, apart from interacting with water, the photoexcited holes produced upon near

UV illumination (i.e. 380 nm) of the VB of QDs can flow into the VB of $LaPO_4$: Ce in a non-radiative fashion, prior to their recombination with photogenerated electrons in the QDs. By contrast, under deep UV light irradiation (i.e. 260 nm), the CB levels of LP-Ce are higher in energy than the corresponding CB of CdSe, and therefore, excited electrons in LP-Ce can rather favorably flow into the CB of CdSe QDs, thereby resulting in a significant reduction of the inherent PL emission of Ce^{3+} incorporated as part of $LaPO_4$ (Figure 12C).

By means of comparison, for ions such as Eu^{3+} and Tb^{3+}, the energy gap between the ground state (VB) of the $4f^n$ configuration and the lowest energy level of the $4f^{n-1}5d^1$ configuration is filled with excited state levels, arising from the $4f^n$ configuration, as shown in Figure 13. Such ions will consequently display line spectra associated with radiative transitions, characteristic of $4f^n$ states, as shown in Figure 10D. Moreover, the VB of Eu^{3+} and Tb^{3+} in $LaPO_4$ (i.e. ~-9.0 eV for Eu^{3+} and i.e. ~-7.7 eV for Tb^{3+}) is located below that of CdSe QDs (i.e. -6.1 eV), such that it is not necessarily ideal for charge transfer to occur from CdSe QDs to either LP-Eu or to LP-Tb. However, either charge or energy transfer from LP-Eu and LP-Tb to CdSe QDs is possible, because the CB of LP-Tb and LP-Eu is situated at a level higher than that of CdSe QDs, as shown in Figure 14. However, the efficiency of the charge and/or energy transfer processes from rare-earth ion (i.e. Tb or Eu) doped $LaPO_4$ to CdSe QDs or vice versa in these heterostructures is inherently dependent upon the excitation wavelength. As such, in addition to determining the exact role of the QDs in governing the charge transfer process to water molecules in $LaPO_4$, future studies will revolve around measuring decay kinetics as a function of the excitation wavelength as well as collecting both femtosecond transient absorption and time-resolved PL upconversion data.

4. Conclusions

Nanowires of $LaPO_4$: Re (Re = Ce, Eu, Tb) possessing high-aspect ratios (~7 nm in diameter and ~1.3 μm in length) have been prepared by a modified hydrothermal route, and the corresponding 3D urchin-like sub-micron scale (~ 500 nm diameter) architectures have been generated by a solution-precipitation approach using MHA as a self-assembly facilitating agent. We have found that MHA plays a crucial role in generating sub-micron scale 3D urchin-like spheres, and a corresponding growth mechanism for the formation of 3D structures as a function of growth time and chemical potential has also been suggested.

Our new synthetic strategy for fabricating 3D hierarchical architectures discussed herein represents a facile, reasonably benign, and effective route for the generalized, large-scale *'nanomanufacturing'* of various types of lanthanide, i.e. yttrium and gadolinium, phosphates (either with or without dopants), possessing the same space group as $LaPO_4$. Moreover, pre-formed 0D CdSe QDs, possessing a diameter of ~4.5 nm, have been successfully anchored onto these rare-earth-ion doped $LaPO_4$ 1D nanowires and 3D sub-micron scale architectures to generate the corresponding heterostructures with over 3 times higher QD coverage noted for the 3D material as compared with the 1D wires, as deduced by both EDS spectra and mapping data.

From a photophysical perspective, the resulting nanoscale 1D and 3D heterostructures displayed PL quenching and shortened lifetimes as compared with unbound CdSe QDs, due to photoexcited charge transfer occurring from CdSe QDs to $LaPO_4$: Eu, as mediated by the presence of water molecules within the $LaPO_4$ structure. As an example of the effect of *morphology* in determining optical properties, the CdSe QDs incorporated within these 3D-based doped heterostructures evinced less PL quenching and longer lifetimes as compared with their 1D heterostructure counterparts. This observation was apparent in spite of the increased viability of charge transfer to adjacent water molecules, due in part to the inherently larger quantity of

CdSe QDs attached onto the 3D $LaPO_4$ structural motif. Rather, the more efficient energy transfer process observed from 3D $LaPO_4$: Eu to CdSe QDs, which could be ascribed to the higher QD coverage density and is based upon the considerable spectral overlap of absorption of CdSe QDs and emission of $LaPO_4$: Eu, likely accounted for the noted morphology effect.

Furthermore, the PL quenching and lifetime were also dominated by the identity of *dopants* associated with $LaPO_4$. Specifically, AET-capped CdSe QD - $LaPO_4$: Tb 3D-urchin-based heterostructures displayed both a higher PL intensity and a longer lifetime as compared with analogous Ce and Eu-activated heterostructures, in part due to a more pronounced spectral overlap of its emission band with the absorption profile of CdSe QDs. On the other hand, CdSe QD - $LaPO_4$: Ce heterostructures evinced more substantial PL quenching as well as shorter lifetimes as compared with not only both Eu-doped and Tb-doped heterostructures but also a control sample of AET-capped CdSe QD - undoped $LaPO_4$ heterostructures, thereby indicating that the photoinduced charge transfer process can occur through several complementary channels, i.e. not only through the mediation of water molecules but also through the presence of Ce dopants in $LaPO_4$.

Hence, we suggest that a fundamental understanding of the various charge and energy transfer processes in our model CdSe QD (0D) nanocrystal – rare earth activated $LaPO_4$ 1D nanowire / 3D urchin-like heterostructures can lead to an improved capability to tune the optoelectronic properties of constituent nanomaterials for possible incorporation into functional nanoscale devices. Specifically, these architectures, in which structure, morphology, and chemical composition are treated as ‘variables’ with which to tailor and control optical behavior, offer the opportunity to ‘toggle’ between energy and charge transfer processes. As such, our work is consistent with the idea that highly efficient charge separation can be potentially

promoted by purposely modulating localized chemical interactions within discrete structures, and in so doing, is relevant for the fabrication of more sophisticated photovoltaic constructs.

5. Acknowledgements

Research (including support for JKH, LW, and SSW) was supported by the U.S. Department of Energy, Basic Energy Sciences, Materials Sciences and Engineering Division. Experiments were performed in part at the Center for Functional Nanomaterials located at Brookhaven National Laboratory, which is supported by the U.S. Department of Energy under Contract No. DE-AC02-98CH10886.

Supporting Information Available

Additional structural and optical characterization results as well as lifetime data of our samples are presented. We also present a detailed calculation of the coverage density of CdSe QDs onto both 1D and 3D $LaPO_4$ structures.

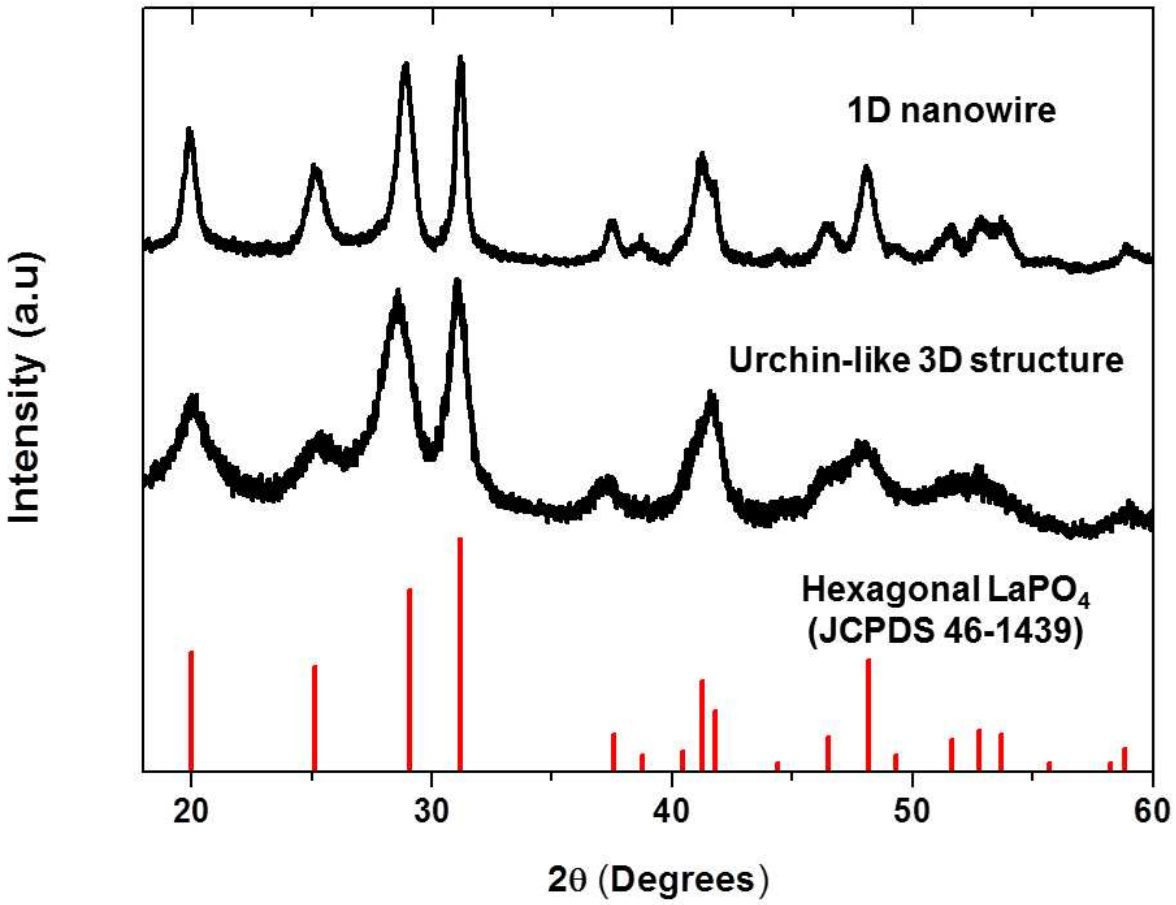

Figure 1. XRD patterns of as-prepared Eu-doped $LaPO_4$ nanowires and the corresponding 3D architecture (top, black). The JCPDS No. 46-1439 database standard is shown for bulk $LaPO_4$ (bottom, red).

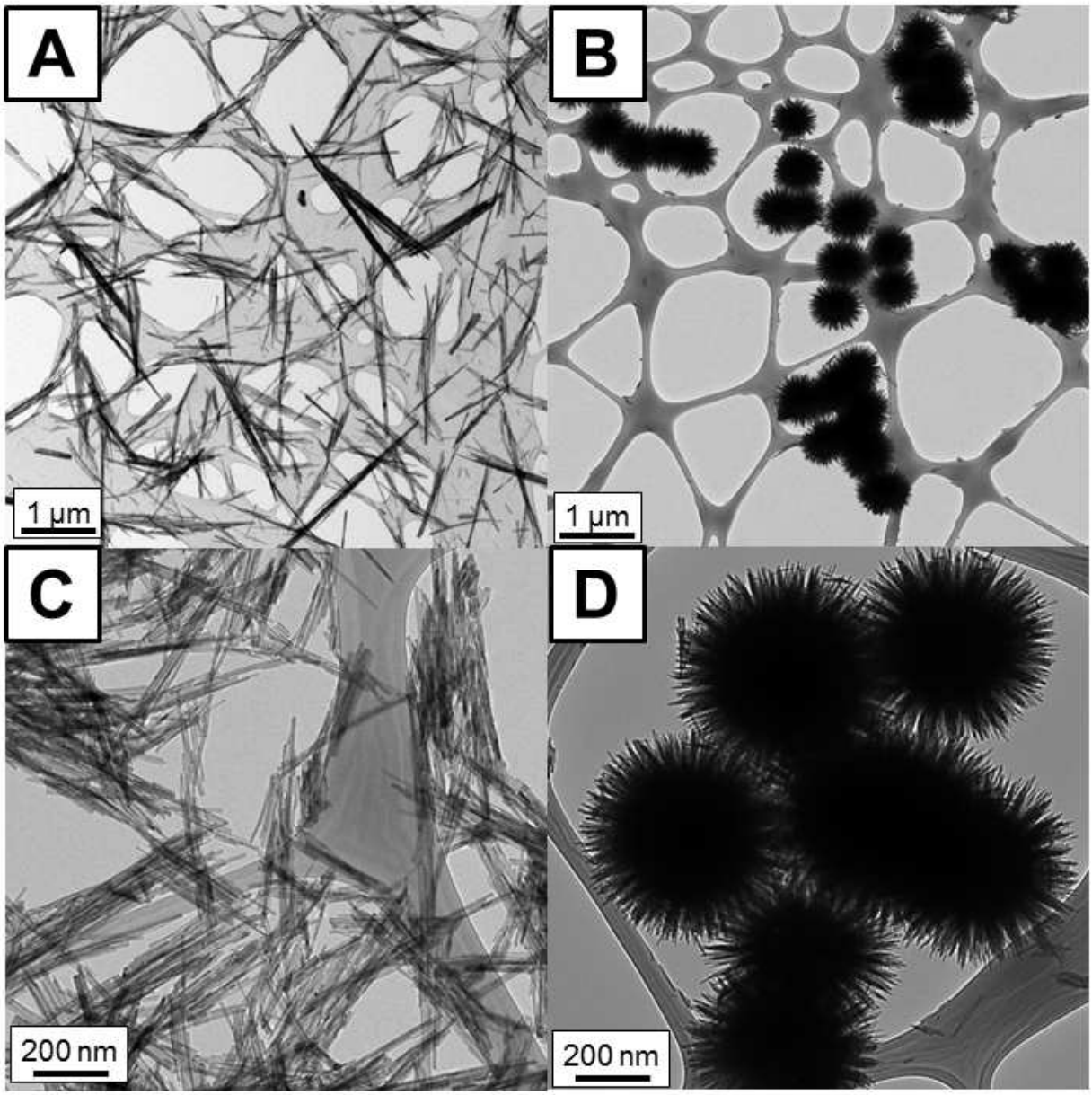

Figure 2. Representative TEM images at lower and higher magnifications of as-prepared $LaPO_4$: Eu (A, C) 1D nanowires and (B, D) 3D urchin-like architectures, respectively.

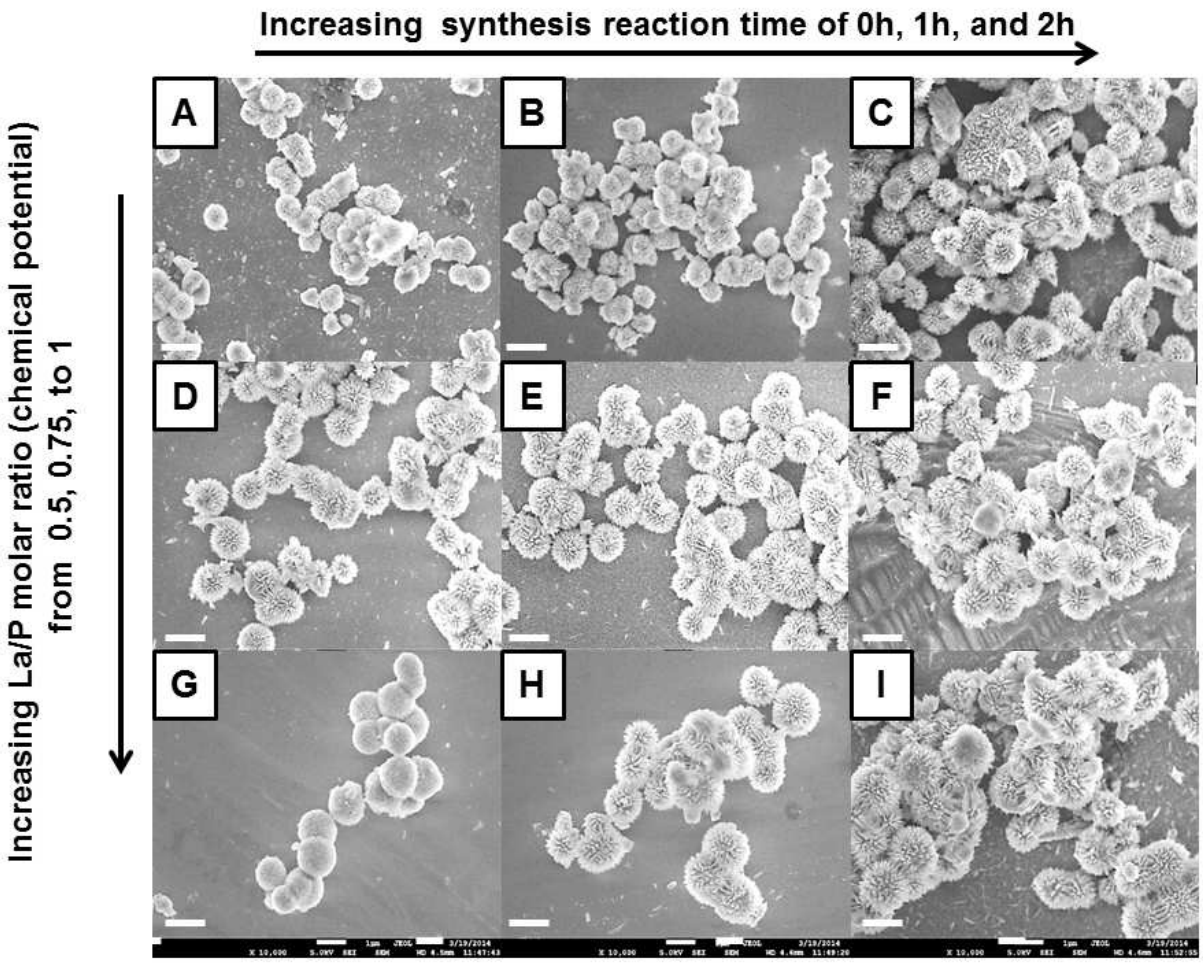

Figure 3. Representative SEM images of 3D $LaPO_4$: Eu architectures formed in the presence of varying precursor La/P ratios (i.e. La/P molar ratios of 0.5, 0.75, and 1) and reaction times (i.e. 0 h, 1 h, and 4 h). ((A), (B), and (C)): constant La/P molar ratio = 0.5 and reaction times of 0 h, 1 h, and 4 h, respectively; ((D), (E), and (F)): constant La/P molar ratio = 0.75 and reaction times of 0 h, 1 h, and 4 h, respectively; ((G), (H), and (I)): constant La/P molar ratio = 1 and reaction times of 0 h, 1 h, and 4 h, respectively. Scale bar is 1 μm in every image.

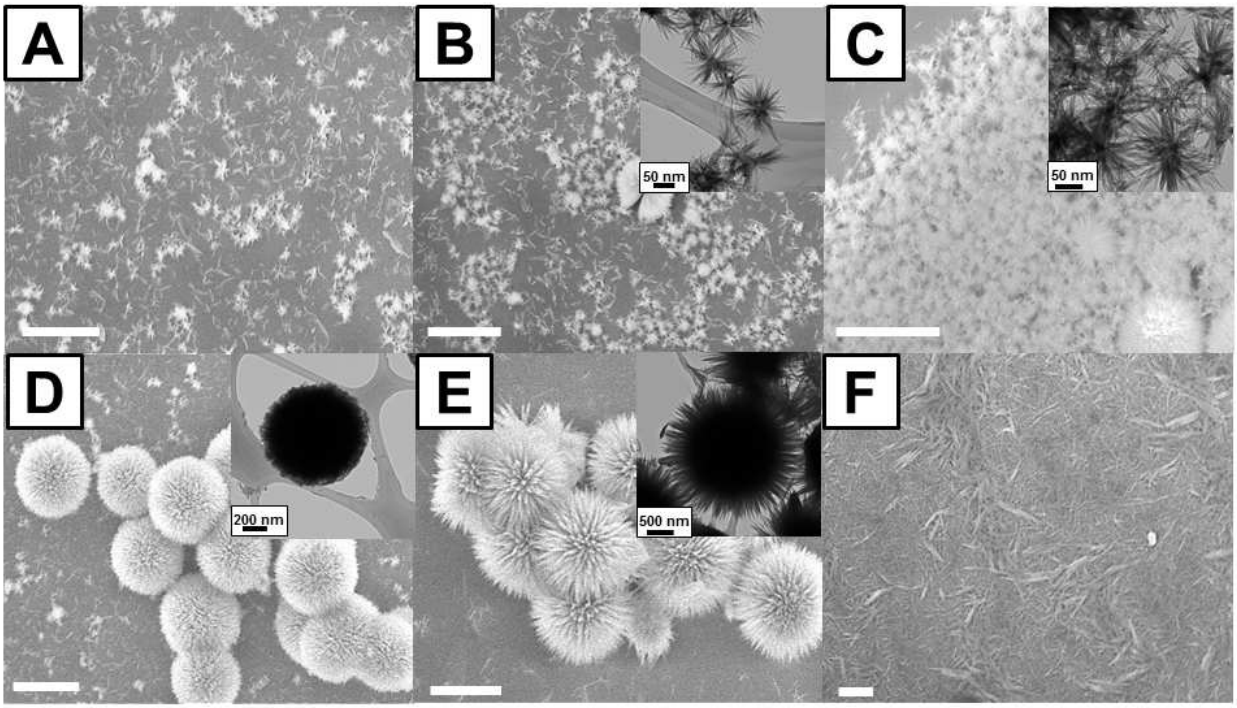

Figure 4. Representative SEM images of a time-dependent evolution (*t* = (A) 0 h, (B) 1 h, (C) 2h, (D) 4h, and (E) 6h) associated with the growth of 3D hierarchical crystal morphologies of $LaPO_4$: Eu in the presence of excess of MHA (molar ratio of MHA: La = 9: 1) at a constant La/P molar ratio of 0.5. Insets to (B), (C), (D), and (E) represent the corresponding TEM images, respectively. (F) SEM image of $LaPO_4$: Eu wire-like nanostructures, prepared in the absence of MHA. The scale bar is 1 μm in every image.

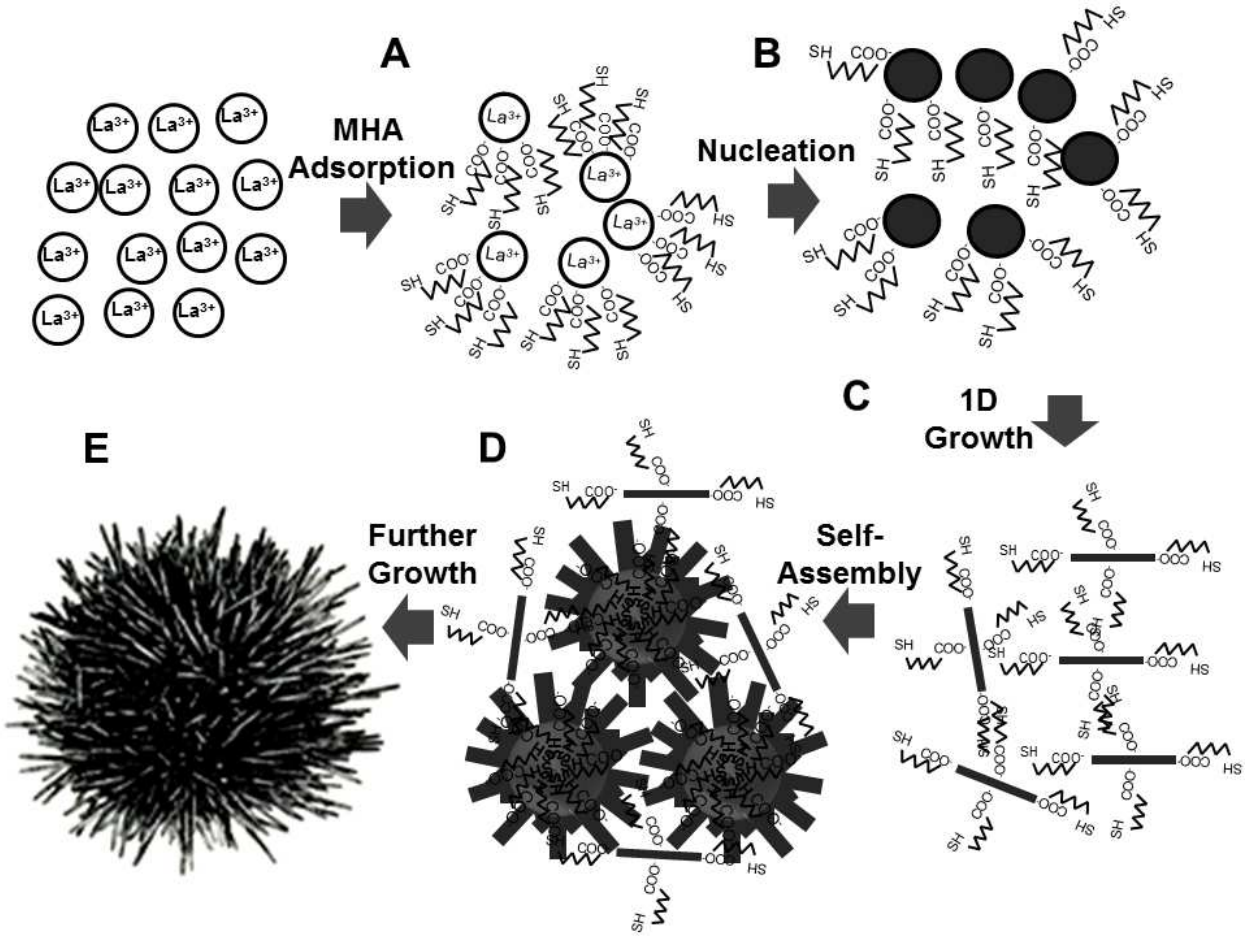

Figure 5. Plausible mechanism for the formation of 3D urchin-like sub-micron scale architectures of $LaPO_4$: Eu.

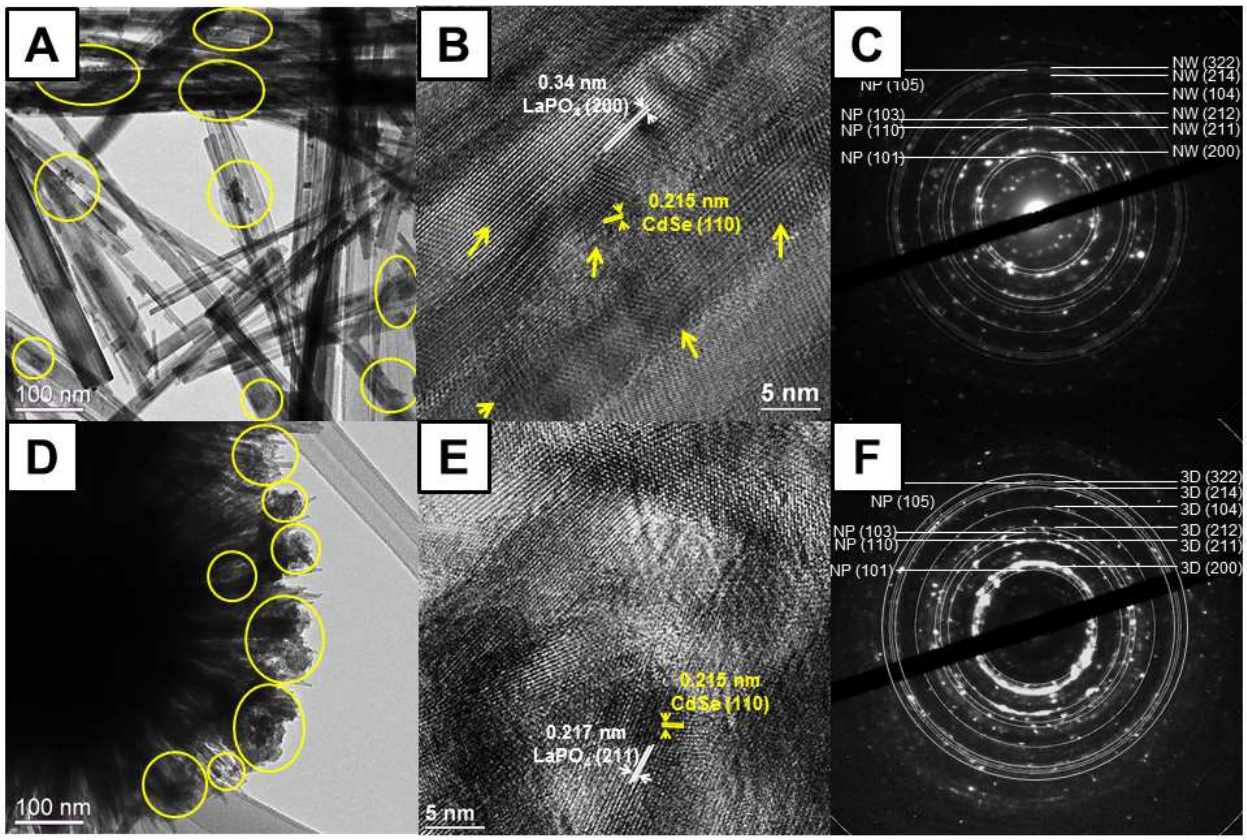

Figure 6. Representative (A and D) TEM and (B and E) HRTEM images, as well as (C and F) SAED patterns, associated with the formation of CdSe QD - $LaPO_4$: Eu 1D and 3D heterostructures, respectively. Yellow circles in (A) and (D) and the corresponding arrows in (B) and (E) highlight regions pertaining to CdSe QDs. In (C) and (F), 'NP' designates CdSe particle reflections whereas 'NW' and '3D' denote the corresponding $LaPO_4$: Eu 1D nanowire and 3D architectural reflections, respectively.

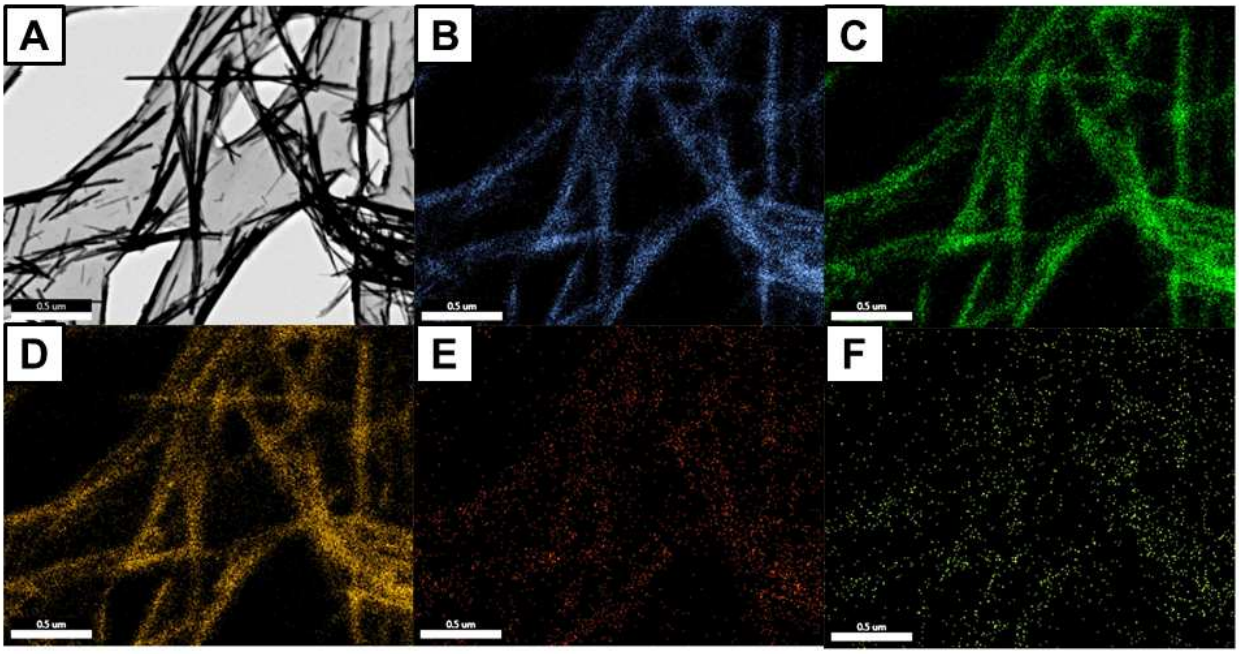

Figure 7. (A) Dark-field STEM image recorded on adjoining CdSe QD - $LaPO_4$: Eu 1D nanowire heterostructures. Elemental mapping of the same region of nanowires, as measured by energy dispersive X-ray spectroscopy using a JEOL JEM-1400 instrument, highlighting the spatial elemental distribution of (B) La (bright blue), (C) P (green), (D) O (dark yellow), (E) Cd (red-brown), and (F) Se (green-yellow), respectively. Scale bar is 500 nm in every image.

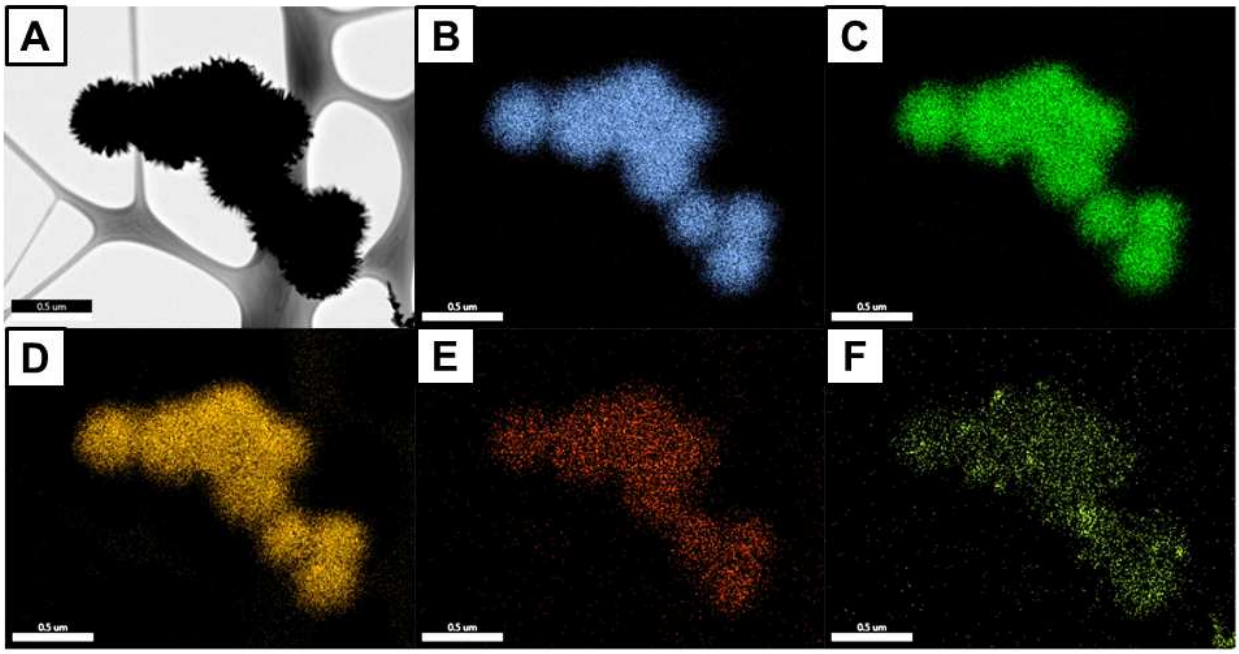

Figure 8. (A) Dark-field STEM image recorded on adjoining CdSe QD - $LaPO_4$: Eu 3D urchin-like heterostructures. Elemental mapping of the same region of 3D-based heterostructures, as measured by energy dispersive X-ray spectroscopy using a JEOL JEM-1400 instrument, highlighting the spatial elemental distribution of (B) La (bright blue), (C) P (green), (D) O (dark yellow), (E) Cd (red-brown), and (F) Se (green-yellow), respectively. Scale bar is 500 nm in every image.

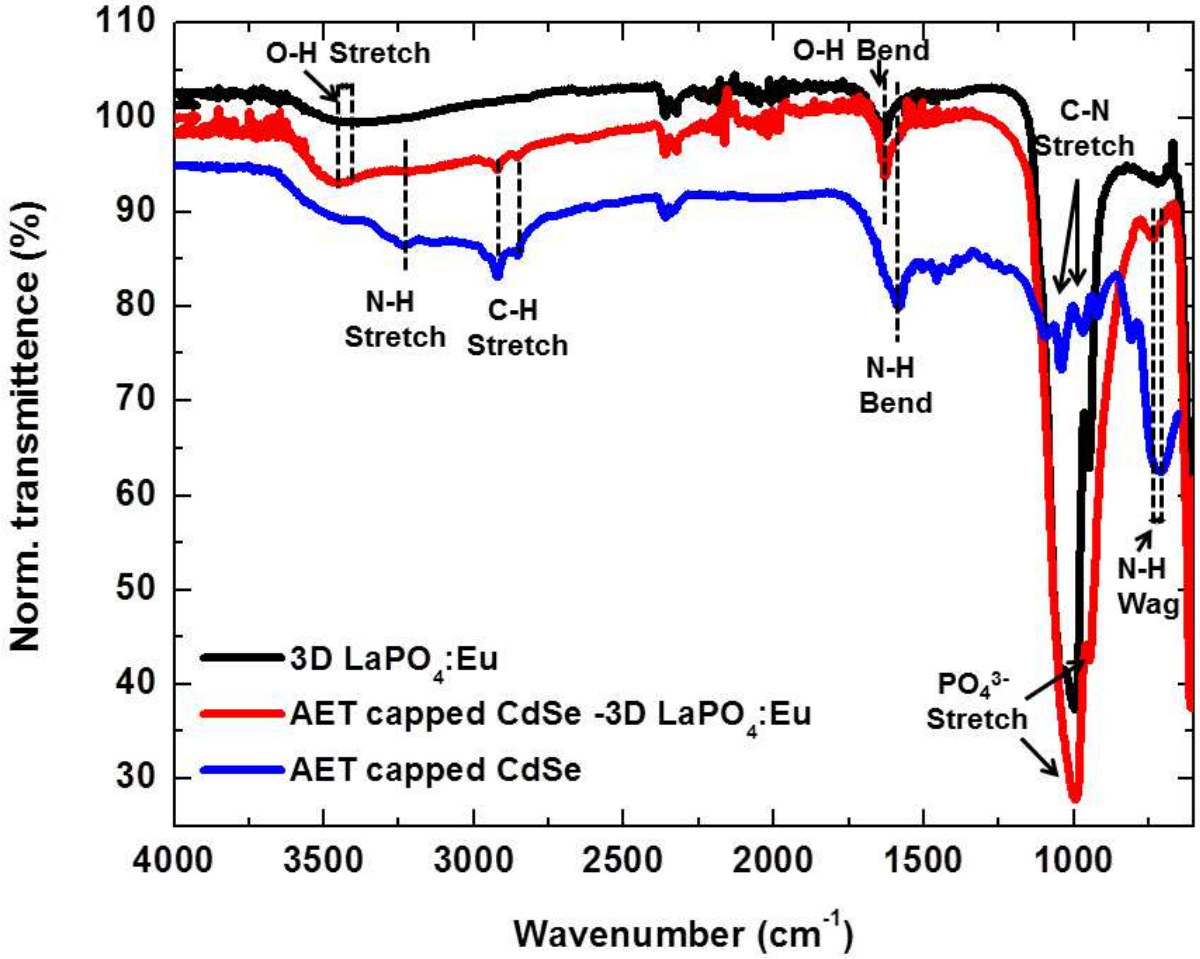

Figure 9. FT-IR spectra of $LaPO_4$: Eu 3D urchin-like structures, AET-capped CdSe QDs, and AET-capped CdSe QD-$LaPO_4$: Eu 3D urchin-like heterostructures.

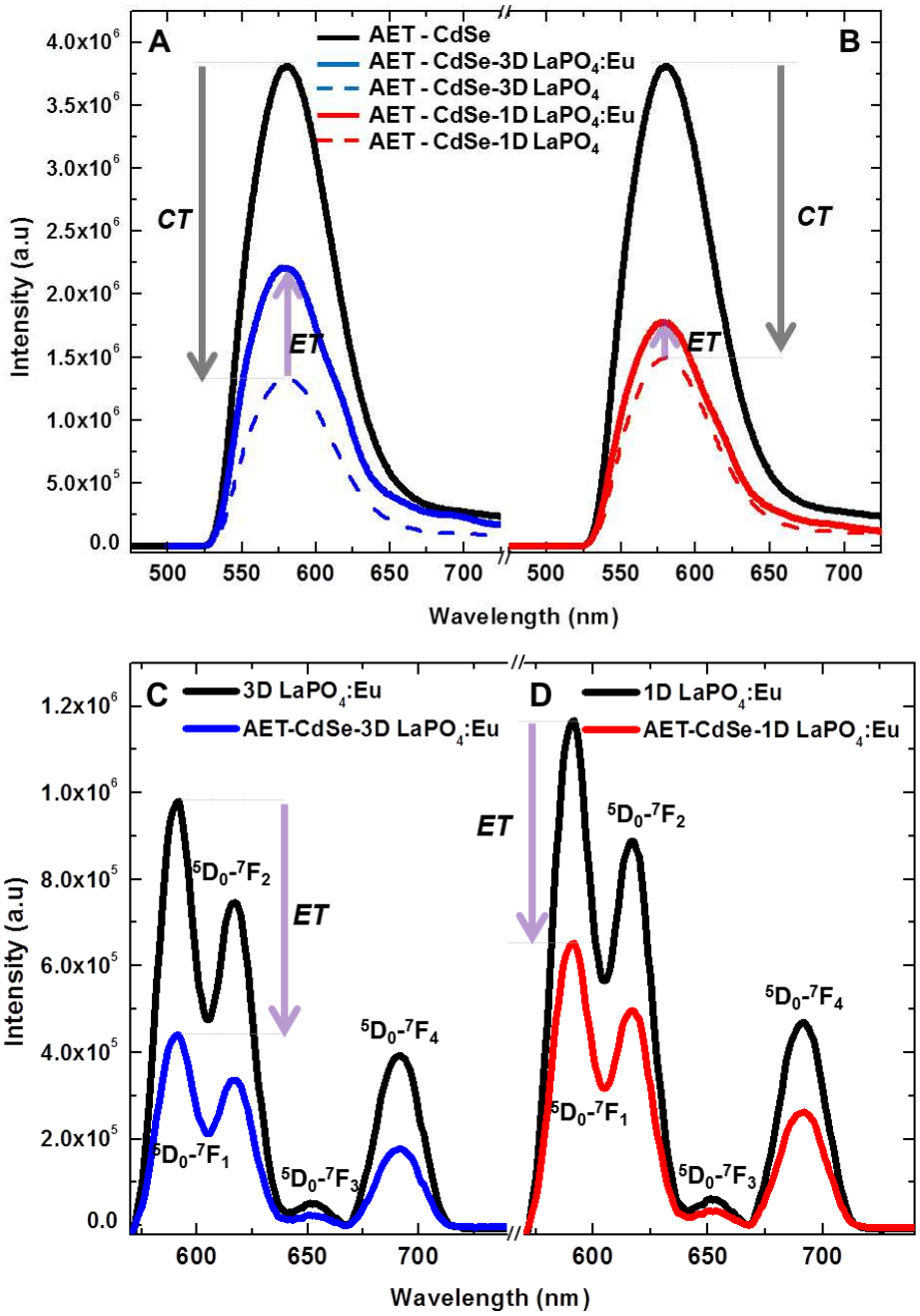

Figure 10. PL emission spectra of (A and C) AET-capped CdSe QDs, AET-capped CdSe QD-3D $LaPO_4$: Eu urchin-like heterostructures, and undoped AET-capped CdSe QD - 3D $LaPO_4$ urchin-like heterostructures under 380 nm and 260 nm excitation, respectively. PL emission spectra of (B and D) AET-capped CdSe QDs, AET-capped CdSe QD- 1D $LaPO_4$: Eu heterostructures, and undoped AET-capped CdSe QD – 1D $LaPO_4$ heterostructures under 380 nm and 260 nm excitation, respectively. Arrows in (A) and (B) indicate PL quenching and enhancement, attributed to charge transfer (CT) and energy transfer (ET) processes, respectively, between CdSe QDs and Eu-activated $LaPO_4$ structures.

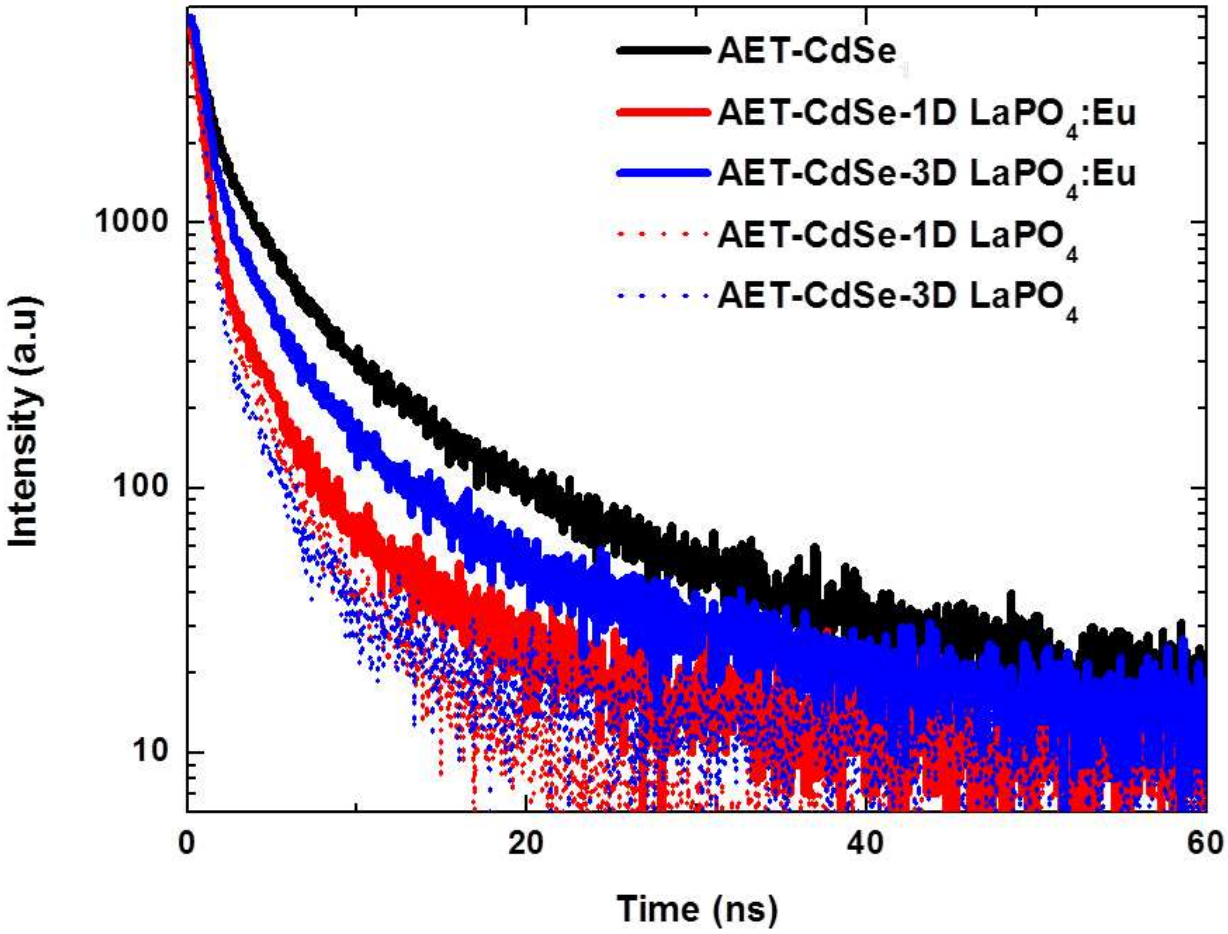

Figure 11. PL decay curves (λ_{ex} = 388 nm) of the excitonic emission of AET-capped CdSe QD emission within AET-capped CdSe QD-$LaPO_4$: Eu heterostructures, incorporating both 1D and 3D structural motifs.

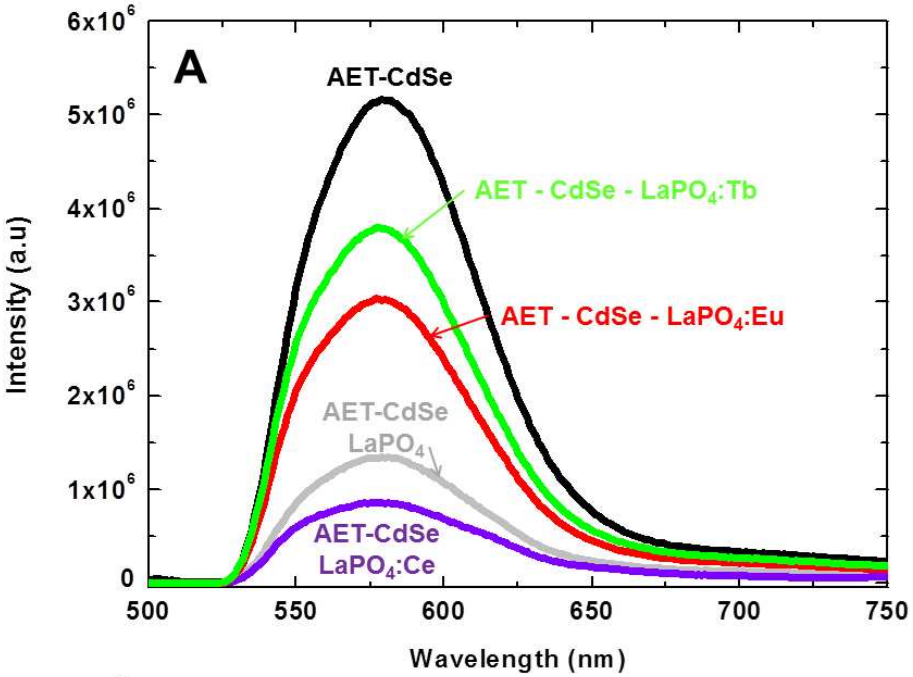
A
AET-CdSe
AET - CdSe - LaPO4:Tb
AET - CdSe - LaPO4:Eu
AET-CdSe
LaPO4
AET-CdSe
LaPO4:Ce
Intensity (a.u)
Wavelength (nm)
6x10^6
5x10^6
4x10^6
3x10^6
2x10^6
1x10^6
0
500
550
600
650
700
750

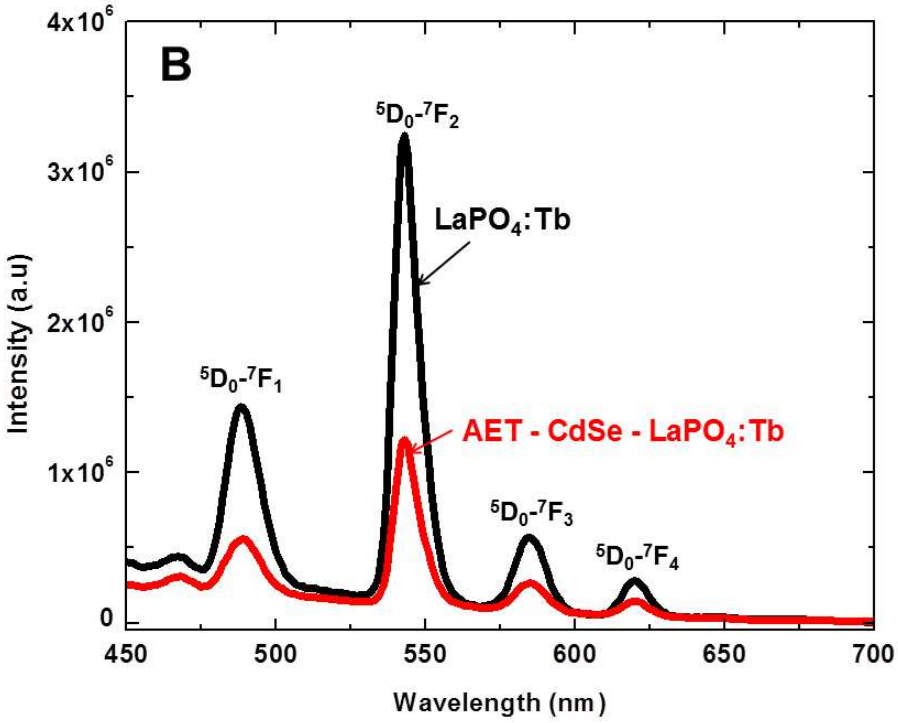
B
5D0-7F2
LaPO4:Tb
5D0-7F1
AET - CdSe - LaPO4:Tb
5D0-7F3
5D0-7F4
Intensity (a.u)
Wavelength (nm)
4x10^6
3x10^6
2x10^6
1x10^6
0
450
500
550
600
650
700

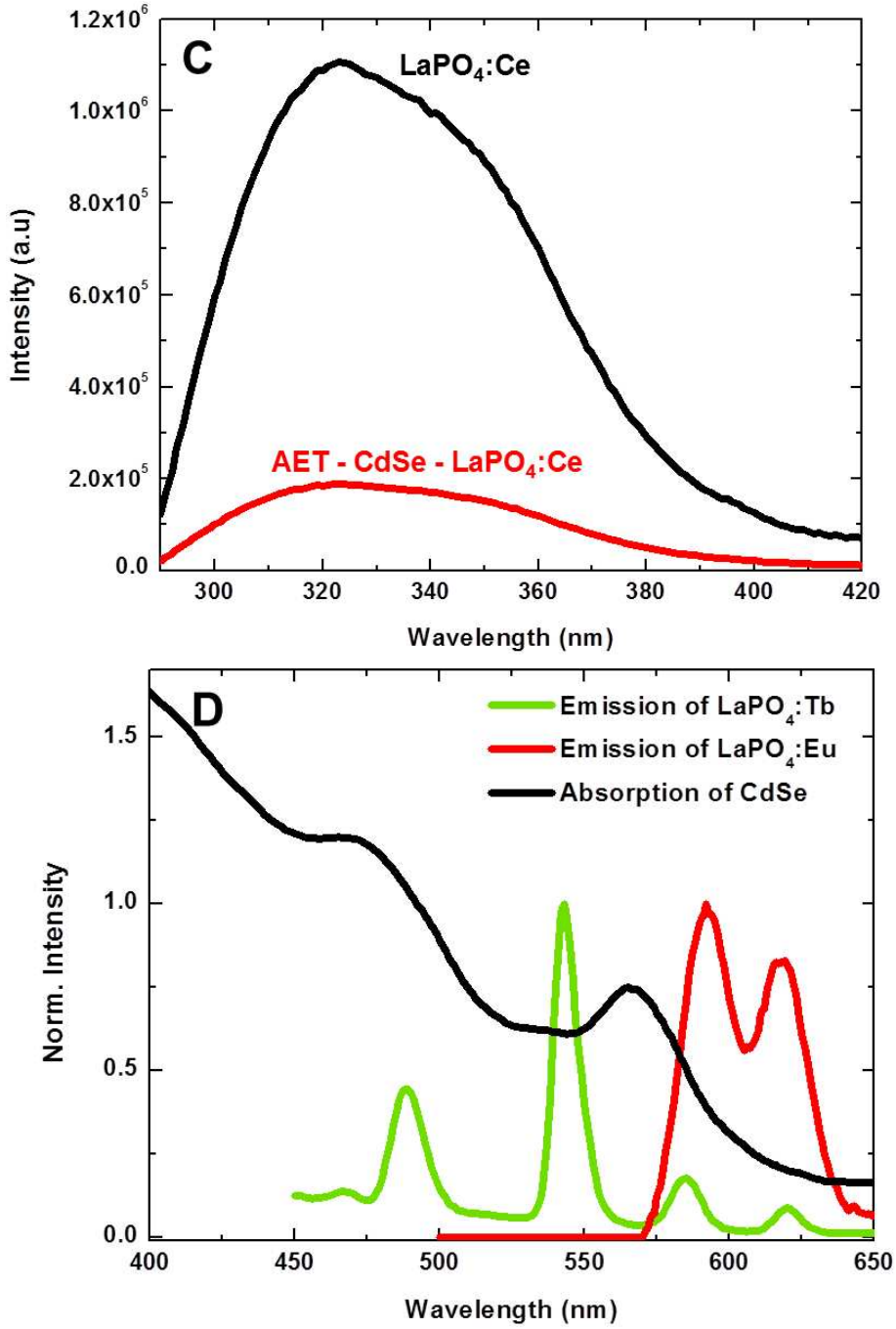

Figure 12. PL emission spectra of (A) AET-capped CdSe QDs as well as of AET-capped CdSe QDs coupled with either $LaPO_4$, $LaPO_4$: Eu, $LaPO_4$: Tb, or $LaPO_4$: Ce as components of 3D-urchin-based heterostructures, excited at 380 nm. PL emission spectra of (B) $LaPO_4$: Tb and AET-capped CdSe QD - $LaPO_4$: Tb 3D-urchin-based heterostructures as well as of (C) $LaPO_4$: Ce and AET-capped CdSe QD - $LaPO_4$: Ce 3D-urchin-based heterostructures, excited at 260 nm. (D) Spectral overlap of the emission spectra of $LaPO_4$: Eu and $LaPO_4$: Tb coupled with the absorption profile of CdSe QDs.

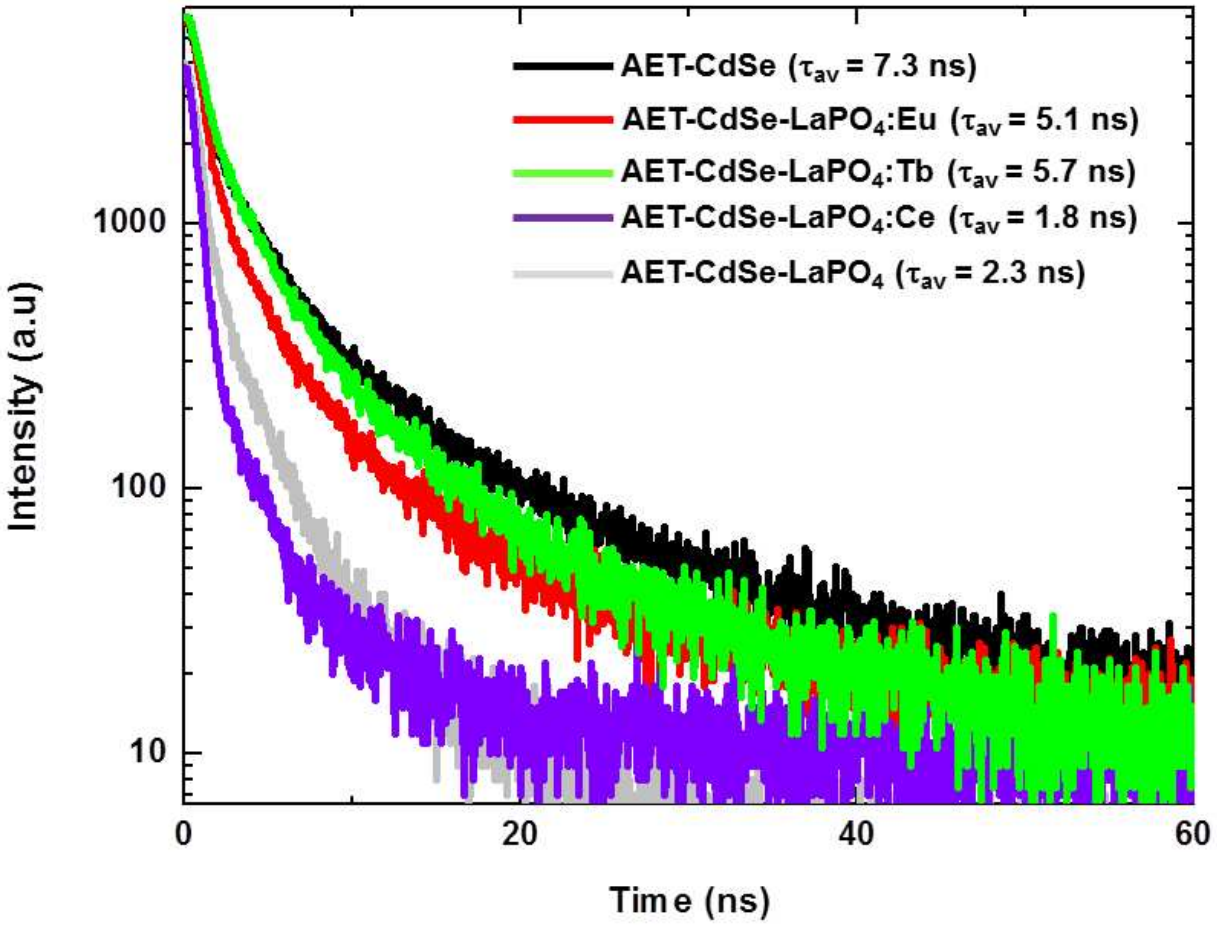

Figure 13. PL decay curves (λ_{ex} = 388 nm) associated with the excitonic emission of AET-capped CdSe QDs in heterostructures, composed of AET-capped CdSe QDs, coupled with 3D motifs of $LaPO_4$, $LaPO_4$: Ce, $LaPO_4$: Eu, and $LaPO_4$: Tb, respectively.

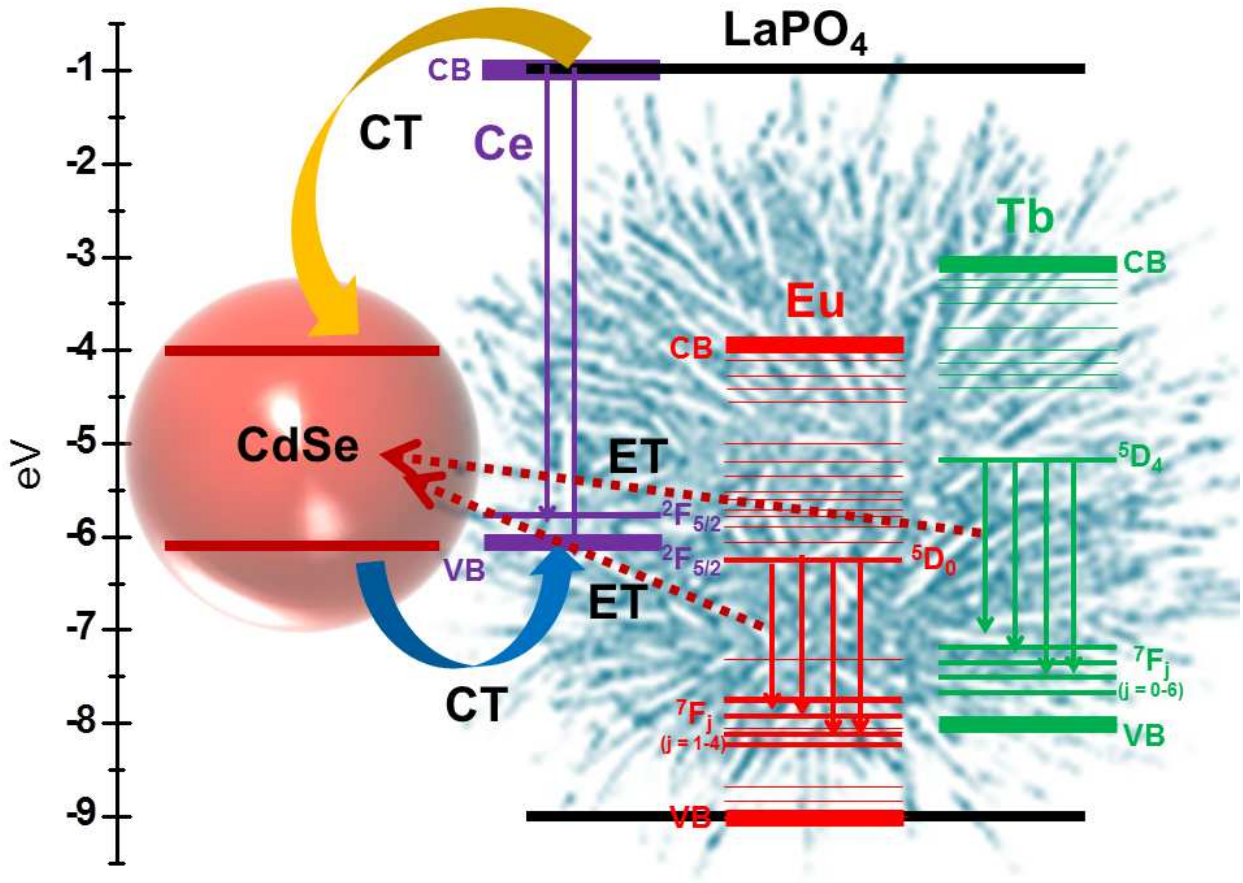

Figure 14. Electronic energy diagram describing the energy band alignments associated with heterostructures composed of CdSe QDs attached to $LaPO_4$, $LaPO_4$: Ce, $LaPO_4$: Eu, and $LaPO_4$: Tb, respectively, as well as the corresponding charge (CT) and energy transfer (ET) schematics in these materials. CB = conduction band and VB = valence band.

References

1. T. Zhai, X. Fang, Y. Bando, Q. Liao, X. Xu, H. Zeng, Y. Ma, J. Yao and D. Golberg, *ACS Nano*, 2009, **3**, 949-959.
2. Tana, M. Zhang, J. Li, H. Li, Y. Li and W. Shen, *Catalysis Today*, 2009, **148**, 179-183.
3. M.-S. Park, Y.-M. Kang, G.-X. Wang, S.-X. Dou and H.-K. Liu, *Advanced Functional Materials*, 2008, **18**, 455-461.
4. Y. Mao and S. S. Wong, *Journal of the American Chemical Society*, 2006, **128**, 8217-8226.
5. S.-K. Kim, R. W. Day, J. F. Cahoon, T. J. Kempa, K.-D. Song, H.-G. Park and C. M. Lieber, *Nano Letters*, 2012, **12**, 4971-4976.
6. A. Salant, M. Shalom, Z. Tachan, S. Buhbut, A. Zaban and U. Banin, *Nano Letters*, 2012, **12**, 2095-2100.
7. A. McLaren, T. Valdes-Solis, G. Li and S. C. Tsang, *Journal of the American Chemical Society*, 2009, **131**, 12540-12541.
8. N. J. Borys, M. J. Walter, J. Huang, D. V. Talapin and J. M. Lupton, *Science*, 2010, **330**, 1371-1374.
9. X. Chen and S. S. Mao, *Chemical reviews*, 2007, **107**, 2891-2959.
10. S. Guo and E. Wang, *Nano Today*, 2011, **6**, 240-264.
11. T. K. Sau and A. L. Rogach, *Advanced Materials*, 2010, **22**, 1781-1804.
12. S. Banerjee and S. S. Wong, *Nano Letters*, 2002, **2**, 195-200.
13. X. Peng, J. Chen, J. A. Misewich and S. S. Wong, *Chemical Society Reviews*, 2009, **38**, 1076-1098.
14. S. Banerjee and S. S. Wong, *Journal of the American Chemical Society*, 2003, **125**, 10342-10350.
15. X. Peng, M. Y. Sfeir, F. Zhang, J. A. Misewich and S. S. Wong, *The Journal of Physical Chemistry C*, 2010, **114**, 8766-8773.
16. X. Peng, J. A. Misewich, S. S. Wong and M. Y. Sfeir, *Nano Letters*, 2011, **11**, 4562-4568.
17. L. Ge and J. Liu, *Applied Catalysis B: Environmental*, 2011, **105**, 289-297.
18. L. Wang, H. Wei, Y. Fan, X. Gu and J. Zhan, *The Journal of Physical Chemistry C*, 2009, **113**, 14119-14125.
19. B. J. Landi, S. L. Castro, H. J. Ruf, C. M. Evans, S. G. Bailey and R. P. Raffaelle, *Solar Energy Materials and Solar Cells*, 2005, **87**, 733-746.
20. X. Peng, J. Chen, J. A. Misewich and S. S. Wong, *Chemical Society Reviews*, 2009, **38**, 1076-1098.
21. K. S. Leschkies, R. Divakar, J. Basu, E. Enache-Pommer, J. E. Boercker, C. B. Carter, U. R. Kortshagen, D. J. Norris and E. S. Aydil, *Nano Letters*, 2007, **7**, 1793-1798.
22. A. Kongkanand, K. Tvrdy, K. Takechi, M. Kuno and P. V. Kamat, *Journal of the American Chemical Society*, 2008, **130**, 4007-4015.
23. I. Robel, V. Subramanian, M. Kuno and P. V. Kamat, *Journal of the American Chemical Society*, 2006, **128**, 2385-2393.
24. L. Shi, B. Hernandez and M. Selke, *Journal of the American Chemical Society*, 2006, **128**, 6278-6279.
25. C. Yan, A. Dadvand, F. Rosei and D. F. Perepichka, *Journal of the American Chemical Society*, 2010, **132**, 8868-8869.
26. A. Kar, A. Datta and A. Patra, *Journal of Materials Chemistry*, 2010, **20**, 916-922.
27. L. J. Charbonnière, N. Hildebrandt, R. F. Ziessel and H.-G. Löhmannsröben, *Journal of the American Chemical Society*, 2006, **128**, 12800-12809.
28. J. Han, L. Wang and S. S. Wong, *The Journal of Physical Chemistry C*, 2014, **118**, 5671-5682.
29. V. Buissette, M. Moreau, T. Gacoin, J.-P. Boilot, J.-Y. Chane-Ching and T. Le Mercier, *Chemistry of Materials*, 2004, **16**, 3767-3773.
30. Z. Fu and W. Bu, *Solid State Sciences*, 2008, **10**, 1062-1067.

31. J. Kim, A. de la Cotte, R. Deloncle, S. Archambeau, C. Biver, J.-P. Cano, K. Lahlil, J.-P. Boilot, E. Grelet and T. Gacoin, *Advanced Functional Materials*, 2012, **22**, 4949-4956.
32. G. Blasse and B. C. Grabmaier, *Luminescent materials*, Springer, Berlin, 1994.
33. Z. Yin, Y. Sakamoto, J. Yu, S. Sun, O. Terasaki and R. Xu, *Journal of the American Chemical Society*, 2004, **126**, 8882-8883.
34. L. Xu, H. Song, B. Dong, Y. Wang, X. Bai, G. Wang and Q. Liu, *The Journal of Physical Chemistry C*, 2009, **113**, 9609-9615.
35. Z. Huo, C. Chen, D. Chu, H. Li and Y. Li, *Chemistry – A European Journal*, 2007, **13**, 7708-7714.
36. M. Yang, H. You, K. Liu, Y. Zheng, N. Guo and H. Zhang, *Inorganic Chemistry*, 2010, **49**, 4996-5002.
37. W. Li and J. Lee, *The Journal of Physical Chemistry C*, 2008, **112**, 11679-11684.
38. C. Minhua, H. Changwen, W. Qingyin, G. Caixin, Q. Yanjuan and W. Enbo, *Nanotechnology*, 2005, **16**, 282.
39. Y.-P. Fang, A.-W. Xu, R.-Q. Song, H.-X. Zhang, L.-P. You, J. C. Yu and H.-Q. Liu, *Journal of the American Chemical Society*, 2003, **125**, 16025-16034.
40. Y.-W. Zhang, Z.-G. Yan, L.-P. You, R. Si and C.-H. Yan, *European Journal of Inorganic Chemistry*, 2003, **2003**, 4099-4104.
41. W. Bu, L. Zhang, Z. Hua, H. Chen and J. Shi, *Crystal Growth & Design*, 2007, **7**, 2305-2309.
42. X. Zhang, M. Zhang, Y. Zhu, P. Wang, F. Xue, J. Gu, H. Bi and Y. Qian, *Materials Research Bulletin*, 2010, **45**, 1324-1329.
43. M. Yang, H. You, Y. Zheng, K. Liu, G. Jia, Y. Song, Y. Huang, L. Zhang and H. Zhang, *Inorganic Chemistry*, 2009, **48**, 11559-11565.
44. A. I. Becerro, S. Rodríguez-Liviano, A. J. Fernández-Carrión and M. Ocaña, *Crystal Growth & Design*, 2012, **13**, 526-535.
45. Z. Xu, Y. Cao, C. Li, P. a. Ma, X. Zhai, S. Huang, X. Kang, M. Shang, D. Yang, Y. Dai and J. Lin, *Journal of Materials Chemistry*, 2011, **21**, 3686-3694.
46. Z. Xu, C. Li, G. Li, R. Chai, C. Peng, D. Yang and J. Lin, *The Journal of Physical Chemistry C*, 2010, **114**, 2573-2582.
47. L. Qu and X. Peng, *Journal of the American Chemical Society*, 2002, **124**, 2049-2055.
48. R. Mooney, *Acta Crystallographica*, 1950, **3**, 337-340.
49. A. Hezel and S. D. Ross, *Spectrochimica Acta*, 1966, **22**, 1949-1961.
50. M. N. Luwang, R. S. Ningthoujam, S. K. Srivastava and R. K. Vatsa, *Journal of the American Chemical Society*, 2011, **133**, 2998-3004.
51. Z. A. Peng and X. Peng, *Journal of the American Chemical Society*, 2001, **123**, 1389-1395.
52. Z. A. Peng and X. Peng, *Journal of the American Chemical Society*, 2002, **124**, 3343-3353.
53. G. M. Pound and V. K. L. Mer, *Journal of the American Chemical Society*, 1952, **74**, 2323-2332.
54. Z. Li and Y. Zhang, *Angewandte Chemie International Edition*, 2006, **45**, 7732-7735.
55. Q. Gong, X. Qian, X. Ma and Z. Zhu, *Crystal Growth & Design*, 2006, **6**, 1821-1825.
56. Q. Wang, B. Liu, X. Wang, S. Ran, L. Wang, D. Chen and G. Shen, *Journal of Materials Chemistry*, 2012, **22**, 21647-21653.
57. S. Song, R. A. Clark, E. F. Bowden and M. J. Tarlov, *The Journal of Physical Chemistry*, 1993, **97**, 6564-6572.
58. D. H. Murgida and P. Hildebrandt, *Chemical Society Reviews*, 2008, **37**, 937-945.
59. O. M. Bakr, B. H. Wunsch and F. Stellacci, *Chemistry of Materials*, 2006, **18**, 3297-3301.
60. N. Zhang, W. Bu, Y. Xu, D. Jiang and J. Shi, *The Journal of Physical Chemistry C*, 2007, **111**, 5014-5019.
61. Z. Xu, X. Kang, C. Li, Z. Hou, C. Zhang, D. Yang, G. Li and J. Lin, *Inorganic Chemistry*, 2010, **49**, 6706-6715.

62. R. Vanyúr, L. Biczók and Z. Miskolczy, *Colloids and Surfaces A: Physicochemical and Engineering Aspects*, 2007, **299**, 256-261.
63. T. Wallin and P. Linse, *The Journal of Physical Chemistry B*, 1997, **101**, 5506-5513.
64. Z. Sun, J. H. Kim, Y. Zhao, F. Bijarbooneh, V. Malgras, Y. Lee, Y.-M. Kang and S. X. Dou, *Journal of the American Chemical Society*, 2011, **133**, 19314-19317.
65. M. Xu, L. Kong, W. Zhou and H. Li, *The Journal of Physical Chemistry C*, 2007, **111**, 19141-19147.
66. P. Yu, X. Zhang, D. Wang, L. Wang and Y. Ma, *Crystal Growth & Design*, 2008, **9**, 528-533.
67. L.-P. Zhu, H.-M. Xiao, X.-M. Liu and S.-Y. Fu, *Journal of Materials Chemistry*, 2006, **16**, 1794-1797.
68. X. Peng, M. Y. Sfeir, F. Zhang, J. A. Misewich and S. S. Wong, *The Journal of Physical Chemistry C*, 2010, **114**, 8766-8773.
69. S. Ji, T. Jiang, K. Xu and S. Li, *Applied Surface Science*, 1998, **133**, 231-238.
70. T. Gramstad, *Spectrochimica Acta*, 1963, **19**, 829-834.
71. K. Pechstedt, T. Whittle, J. Baumberg and T. Melvin, *The Journal of Physical Chemistry C*, 2010, **114**, 12069-12077.
72. D. Pieter, *Journal of Physics: Condensed Matter*, 2013, **25**, 225501.
73. K. T. Shimizu, W. K. Woo, B. R. Fisher, H. J. Eisler and M. G. Bawendi, *Physical Review Letters*, 2002, **89**, 117401.
74. N. Hildebrandt, L. J. Charbonniere and H.-G. Lohmannsroben, *Journal of Biomedicine and Biotechnology*, 2007, **2007**.
75. H. Song, Y. Zhu, S. Cui, X. Chen, W. Xu, P. Zhou, Y. Wang, L. Xu, L. Huang and W. Huang, *Nanoscale*, 2014.
76. J. Fang, C. W. Evans, G. J. Willis, D. Sherwood, Y. Guo, G. Lu, C. L. Raston and K. S. Iyer, *Lab on a Chip*, 2010, **10**, 2579-2582.
77. Y. Tan and C. Shi, *Journal of Physics and Chemistry of Solids*, 1999, **60**, 1805-1810.
78. J. K. Han, M. E. Hannah, A. Piquette, J. B. Talbot, K. C. Mishra and J. McKittrick, *ECS Journal of Solid State Science and Technology*, 2012, **1**, R98-R102.
79. K. Y. Jung, C. H. Lee and Y. C. Kang, *Materials Letters*, 2005, **59**, 2451-2456.
80. D. Tonti, F. van Mourik and M. Chergui, *Nano Letters*, 2004, **4**, 2483-2487.